TOPICAL REVIEW

Macroscopically aligned carbon nanotubes for flexible and hightemperature electronics, optoelectronics, and thermoelectrics

To cite this article: Weilu Gao et al 2020 J. Phys. D: Appl. Phys. 53 063001

View the article online for updates and enhancements.



IOP ebooks™

Bringing together innovative digital publishing with leading authors from the global scientific community.

Start exploring the collection-download the first chapter of every title for free.

Topical Review

Macroscopically aligned carbon nanotubes for flexible and high-temperature electronics, optoelectronics, and thermoelectrics

Weilu Gao¹, Natsumi Komatsu¹, Lauren W Taylor², Gururaj V Naik¹, Kazuhiro Yanagi³, Matteo Pasquali^{2,4,5,6} and Junichiro Kono^{1,5,6,7}

- Department of Electrical and Computer Engineering, Rice University, Houston, TX, United States of America
- ² Department of Chemical and Biomolecular Engineering, Rice University, Houston, TX, United States of America
- ³ Department of Physics, Tokyo Metropolitan University, Tokyo, Japan
- ⁴ Department of Chemistry, Rice University, Houston, TX, United States of America
- Department of Materials Science and NanoEngineering, Rice University, Houston, TX, United States of America
- ⁶ The Smalley-Curl Institute, Rice University, Houston, TX, United States of America
- Department of Physics and Astronomy, Rice University, Houston, TX, United States of America

E-mail: wg6@rice.edu and weilugao.rice@gmail.com

Received 22 October 2018, revised 15 September 2019 Accepted for publication 10 October 2019 Published 3 December 2019



Abstract

The remarkable flexibility, stable chemical structure, and extraordinary thermal, electrical, and optical properties of carbon nanotubes (CNTs) are promising for a variety of applications in flexible and/or high-temperature electronics, optoelectronics, and thermoelectrics, including wearables, refractory photonics, and waste heat harvesting. However, the long-standing problem in the preparation of CNT ensembles is to maintain the extraordinary properties of individual CNTs on a macroscopic scale; the polydispersity and randomness remain two main challenges. In this topical review, we will discuss three ways of creating wafer-scale aligned CNTs: direct growth of aligned CNTs by chemical vapor deposition, production of ultrahigh-conductivity CNT fibers through solution spinning and coating, and spontaneous formation of wafer-scale aligned CNT films via controlled vacuum filtration. We will then describe flexible and high-temperature applications of these materials, such as flexible CNT broadband detectors, flexible strain sensors, spectrally selective thermal emitters, and thermoelectric devices.

Keywords: flexible, electronics, optoelectronics, thermoelectrics, high-temperature, aligned carbon nanotubes

1

(Some figures may appear in colour only in the online journal)

1. Introduction

Next-generation electronics, photonics, and thermoelectrics demand that devices and systems be directly worn on soft and curved human bodies. Thus, studies on the development of novel and innovative structures of multifunctional materials for wearable electronic systems have been significantly increasing in recent years. Carbon-based nanomaterials, including zero-dimensional (0D) C₆₀ [1], one-dimensional (1D) carbon nanotubes (CNTs) [2], and two-dimensional (2D) graphene [3], have spurred much excitement and interest in nanoscience and nanoengineering. In particular, single-wall CNTs (SWCNTs) provide an ideal 1D material platform with extraordinary chemical, mechanical, electronic, thermal, and optical properties [4-10]. Since the discovery of SWCNTs in 1993 [11, 12], they have been considered model 1D condensed matter systems where fundamental theoretical questions in many-body physics can be addressed [13–24]. They are also extremely promising candidates to unify electronic, optical, and thermal functions in devices, circuits, and systems [25–27]. In this section, we provide a short review of their crystal structure, electronic structure, and mechanical properties.

1.1. Crystal structure

The atomic structures of different members of the carbon nanomaterial family have much in common. They possess the same sp^2 hybridization, where each carbon atom forms three strong σ bonds with their neighbors and the fourth electron forms a delocalized π bond; see figure 1(a). As shown in figure 1(b), graphene consists of a honeycomb lattice of sp^2 -bonded carbon atoms with interatomic bond length a_{C-C} of 0.142 nm. The primitive unit cell consists of two carbon atoms (labeled A and B in figure 1(b)) that contribute two π electrons of fundamental importance in the electrical and optical phenomena observed in graphene. There are three important high-symmetry points in the reciprocal lattice of graphene: Γ -point (the center of the Brillouin zone), M-point, and K-point; see figure 1(c). $\mathbf{a}_{1,2}$ and $\mathbf{b}_{1,2}$ are the primitive lattice vectors in real and reciprocal space, respectively.

SWCNTs can be formed by wrapping a graphene sheet so that the two points connected by a roll-up vector (or chiral vector) \mathbf{C}_h meet, with nanotube diameter $d_t = |\mathbf{C}_h|/2\pi$. The roll-up vector \mathbf{C}_h can be expressed as a linear combination of \mathbf{a}_1 and \mathbf{a}_2 as $n\mathbf{a}_1 + m\mathbf{a}_2$, where n and m are positive integers with $n \ge m$; see figure 1(d). Molecular dynamics simulations have demonstrated that the atomic structure of both SWCNTs and multi-wall carbon nanotubes (MWCNTs) can be sustained even at temperatures above 2000 K [28]. Moreover, CNTs are even air-stable up to 1000 K based on thermogravimetric analysis [29], and the stability can be further improved by annealing to remove defects in CNTs [30]. The ultrastable chemical structure of CNTs makes them an excellent candidate for high-temperature applications.

1.2. Band structure

The chiral indices (n,m) determine the electronic types of SWCNTs, depending on the value of $\nu \equiv (n-m) \mod 3$:

- (i) If $\nu = 0$, the SWCNT is metallic (figure 2(a)). The band structure has no band gap, and there is a finite density of states at the Fermi energy.
- (ii) If $\nu = 1$ or 2, the SWCNT is semiconducting (figure 2(b)) with a band gap of $\sim 0.7 \,\text{eV}/d_t$ (nm).

However, finite curvature in CNTs causes only armchair nanotubes (n=m) to be truly metallic, and other tubes with $\nu=0$ have small, curvature-induced band gaps that scale as $1/d_t^2$ [13, 31, 32]. In all types of SWCNTs, there are peaks, or van Hove singularities, in density of states, characteristic of 1D systems.

In both metallic and semiconducting SWCNTs, there are strong interband optical transitions [10]. The allowed transitions are represented by arrows in figure 2. Strong 1D quantum confinement not only produces concentrated joint densities of states (or van Hove singularities) but also leads to the generation of stable excitons. Both absorption and emission spectra exhibit peaks due to excitons, not due to van Hove singularities, with typical binding energies of 300–700 meV. Emission can be achieved through either optical or electrical excitation, resulting in photoluminescence or electroluminescence, respectively. Because SWCNTs are 1D structures, the direction of carrier scattering is limited to occur only along the nanotube axis, endowing SWCNTs with ultrahigh conductivities. In particular, metallic SWCNTs have exhibited ultralong mean free paths [33], which can be attributed to the absence of backscattering due to Berry's phase [34, 35], making metallic SWCNTs an ideal material for quantum wire interconnections. Furthermore, field effect transistors built from semiconducting SWCNTs have demonstrated a strong electric field effect and showed an extremely high room temperature mobility $> 10^5$ cm² Vs⁻¹ [36]. The optical absorption of semiconducting SWCNTs can also be electrically modulated [37, 38], giving rise to optoelectronics applications.

1.3. Mechanical flexibility

SWCNTs and MWCNTs are not only strong (large tensile strength) and stiff (large Young's modulus) but also remarkably flexible. Iijima and coworkers [39] observed single and multiple kinks when SWCNTs and MWCNTs were bent while being monitored under a high-resolution electron microscope (figure 3). This process was shown reversible up to a very high bending angle. Falvo and coworkers [40] later confirmed that CNTs can also be bent repeatedly using a tip of an atomic force microscope (AFM). Atomistic simulations of the morphology of bent SWCNTs and MWCNTs are in excellent agreement with experimental images [41]. This property originates from the flexibility of the sp^2 network, which can rehybridize when deformed out of plane [5]. Previous

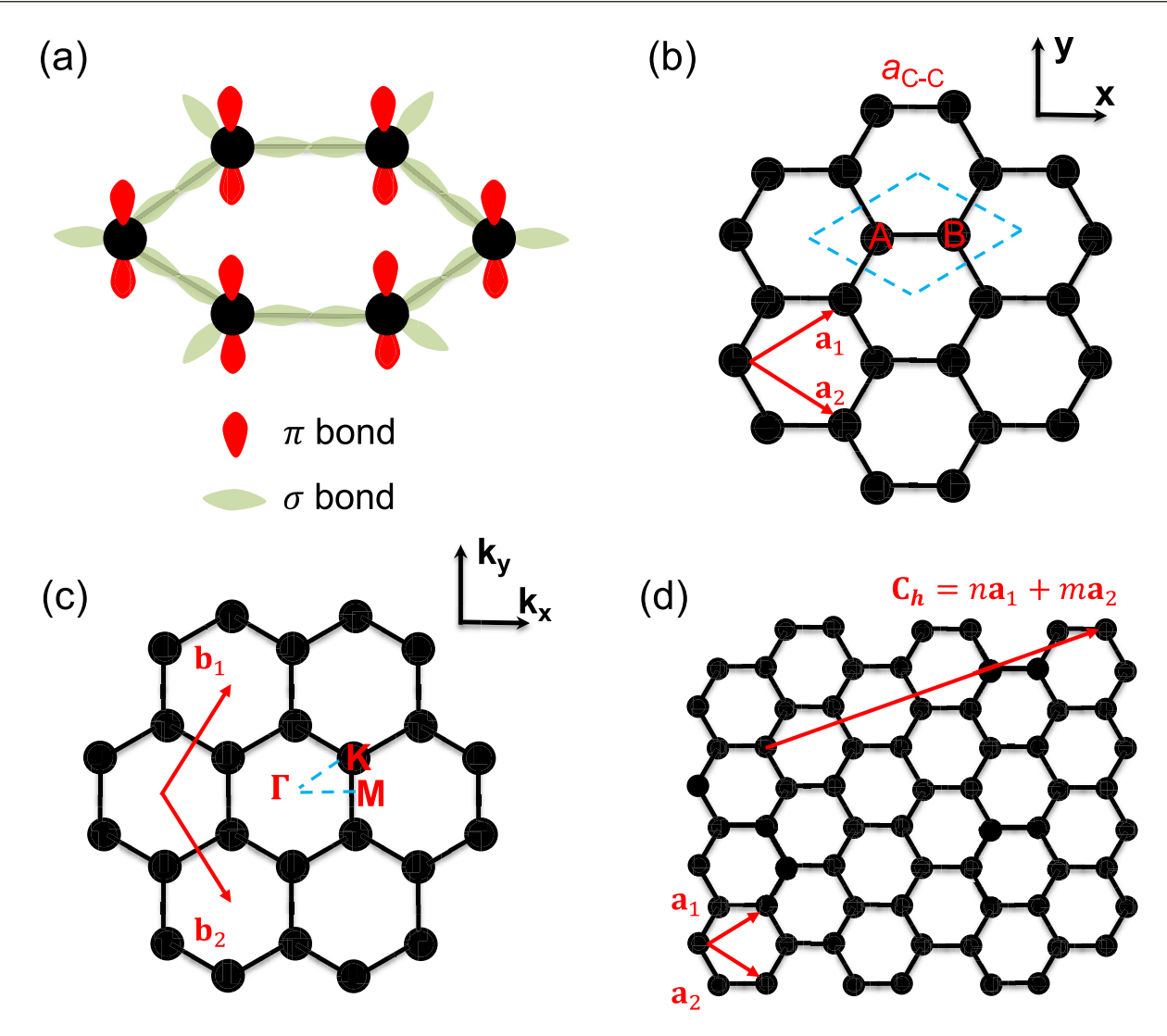


Figure 1. The real and reciprocal lattices of graphene and SWCNTs. (a) Hexagonal bonding in a graphene layer. Black solid dots are carbon nuclei. In-plane σ bonds (light green) and out-of-plane π bonds (red) connect carbon nuclei. (b) Real space and (c) reciprocal space representation of the triangular lattice. a_{C-C} (=0.142 nm) is the carbon–carbon bond length. $a_{1,2}$ and $b_{1,2}$ are the primitive lattice vectors in real and reciprocal space, respectively. The dashed blue line parallelogram defines a unit cell containing two carbon atoms A and B. High-symmetry points of the reciprocal space representation (Γ , M and K) are labeled in the 1st Brillouin zone. (d) A roll-up (or chiral) vector C_h of a SWCNT, connecting two points on graphene, expressed as a linear combination of a_1 and a_2 with integer coefficients n and n. These coefficients are known as the chirality indices of the SWCNT.

experimental studies [42–44] have suggested exceptional mechanical properties of individual CNTs, such as tensile strength >100 GPa and Young's modulus >1 TPa. In recent years, these excellent properties have been extended to macroscopic CNT ensembles, including both CNT fibers and CNT films, through the minimization of defects during production, morphology engineering, and the development of assembly techniques. Large-area CNT films can possess exceptionally high tensile strength 9.6 GPa [45, 46] and Young's modulus approaching 200 GPs [47]. Centimeter-long CNT fibers have achieved 80 GPa tensile strength [48].

As an immediate and significant application of CNTs based on their flexibility, a single MWCNT or a rope of SWCNTs has been used as a tip in scanning probe microscopy, including atomic force microscopy and scanning tunneling microscopy [49]. In contrast to other types of tips, CNT tips can survive tip crashes and maintain their integrity after repeated use. In

addition to this nanoscale application, macroscopic ensembles of CNTs, especially thin films of randomly oriented semiconducting CNTs, have found many applications in large-area, low-cost, flexible, and stretchable electronics, which are difficult or impossible to achieve in semiconductor wafers [50]. Cao and coworkers fabricated high-performance, large-scale, thin-film integrated circuits on plastic substrates (figure 4(a)) based on semiconducting CNTs [51]. Specifically, these transistors displayed mobilities of 80 cm² V⁻¹ s⁻¹, subthreshold slopes of 140 mV dec⁻¹, operating voltages less than 5 V, on/ off ratios of 10⁵, and switching speeds in the kilohertz range. Furthermore, these devices and circuits demonstrated good flexibility without significant change in device performance during inward or outward bending to radii as small as \sim 5 mm [51]. Figure 4(b) shows the normalized transconductance $(g_{\rm m}/g_{\rm m0})$ for a thin-film transistor and normalized voltage gain (G/G_0) for an inverter at different bend radii. Better

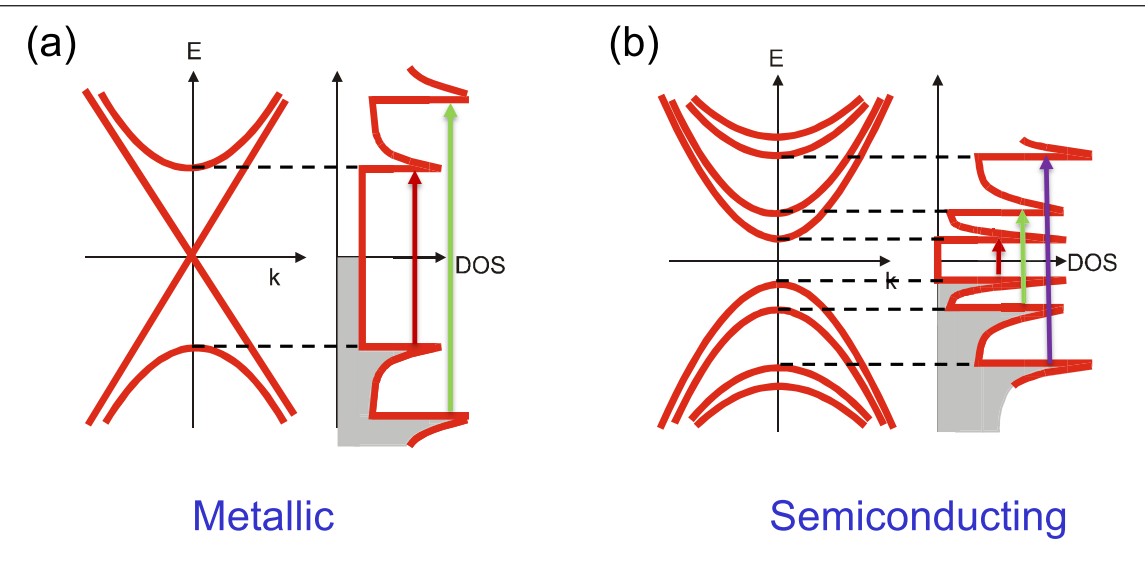


Figure 2. Schematic band structure of (a) metallic and (b) semiconducting SWCNTs.

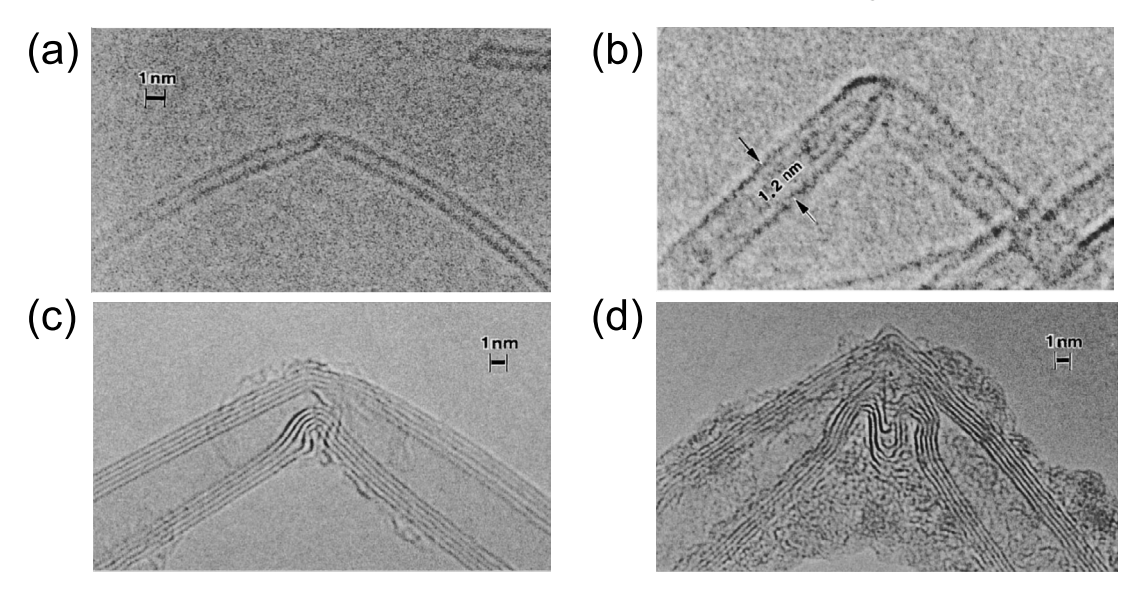


Figure 3. High-resolution electron microscope images of bent carbon nanotubes. (a), (b) A single kink in the middle of a SWCNT with diameters of 0.8 and 1.2 nm, respectively. (c), (d) MWCNT of about 8 nm diameter showing single- and two-kink complexes, respectively. Reprinted from [39], with the permission of AIP Publishing.

control of SWCNT ensemble morphology, density, and alignment, together with enhancement of semiconducting SWCNT purity, further boosted device performance [45, 52–55]. These improvements have also led to other types of devices, including light-emitting devices [56] and skin-like sensors [57].

1.4. Thermoelectric properties

Thermoelectric materials are cost-effective alternatives for harvesting waste heat energy, in which a temperature gradient across the material causes the movement of free carriers generating voltage. The figure of merit for thermoelectric materials, ZT factor, is directly linked to energy conversion efficiency and defined as $S^2\sigma T/\kappa$, where S is the Seebeck coefficient, σ is the electrical conductivity, κ is the thermal conductivity, and T is temperature. Hicks and Dresselhaus predicted that nanomaterials, including CNTs, can offer unprecedented thermoelectric properties, because of the van Hove singularities in

their band structure [58]. Recent progress in the engineering of CNT chirality distribution, carrier density, and morphology in macroscopic ensembles has greatly improved the performance of CNT thermoelectric materials [59, 60]; see recent comprehensive review articles on this topic [61–63].

2. Fabrication of macroscopically aligned CNT samples

To best preserve the extraordinary 1D properties of individual CNTs on a macroscopic scale, it is highly desirable to fabricate assemblies of *aligned* CNTs. Particularly, horizontally aligned CNTs are promising for large-scale integration of electronic and optoelectronic devices. Currently, there are two general categories for producing such materials: (1) *in situ* assembly during CNT growth and (2) *ex situ* assembly after CNT growth. In this article, we highlight three specific

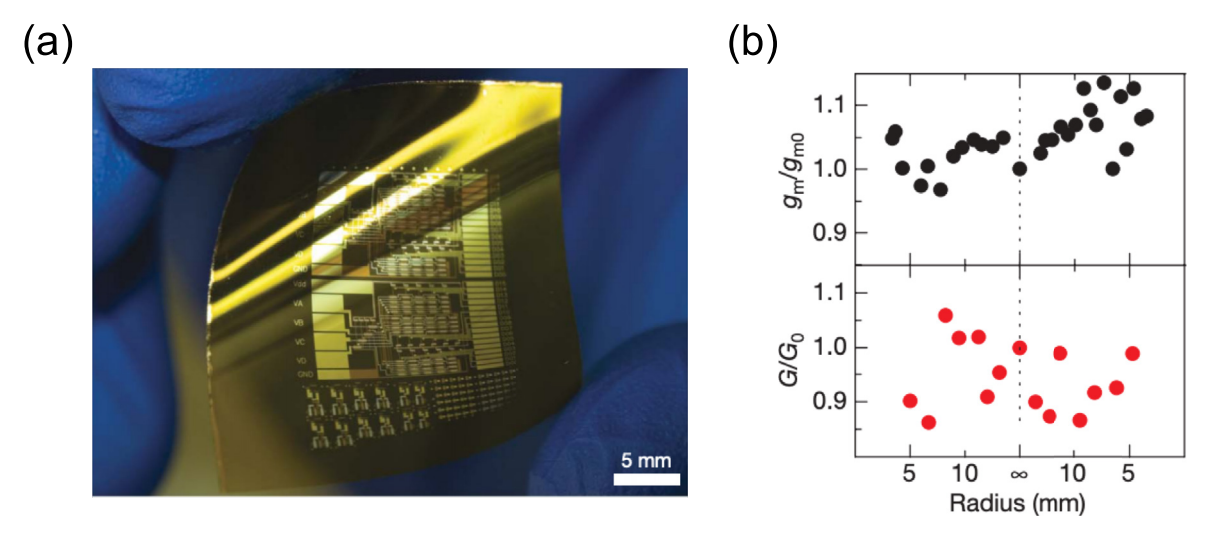


Figure 4. Flexible SWCNT integrated circuits. (a) Photograph of a collection of SWCNT transistors and circuits on a plastic substrate. (b) Plots of $g_{\rm m}/g_{\rm m0}$ (normalized transconductance) for a thin-film transistor and G/G_0 (normalized voltage gain) for an inverter as a function of bend radius. $g_{\rm m0}$ and G_0 denote the responses in the unbent state. [51] Copyright © 2008, Springer Nature. With permission of Springer.

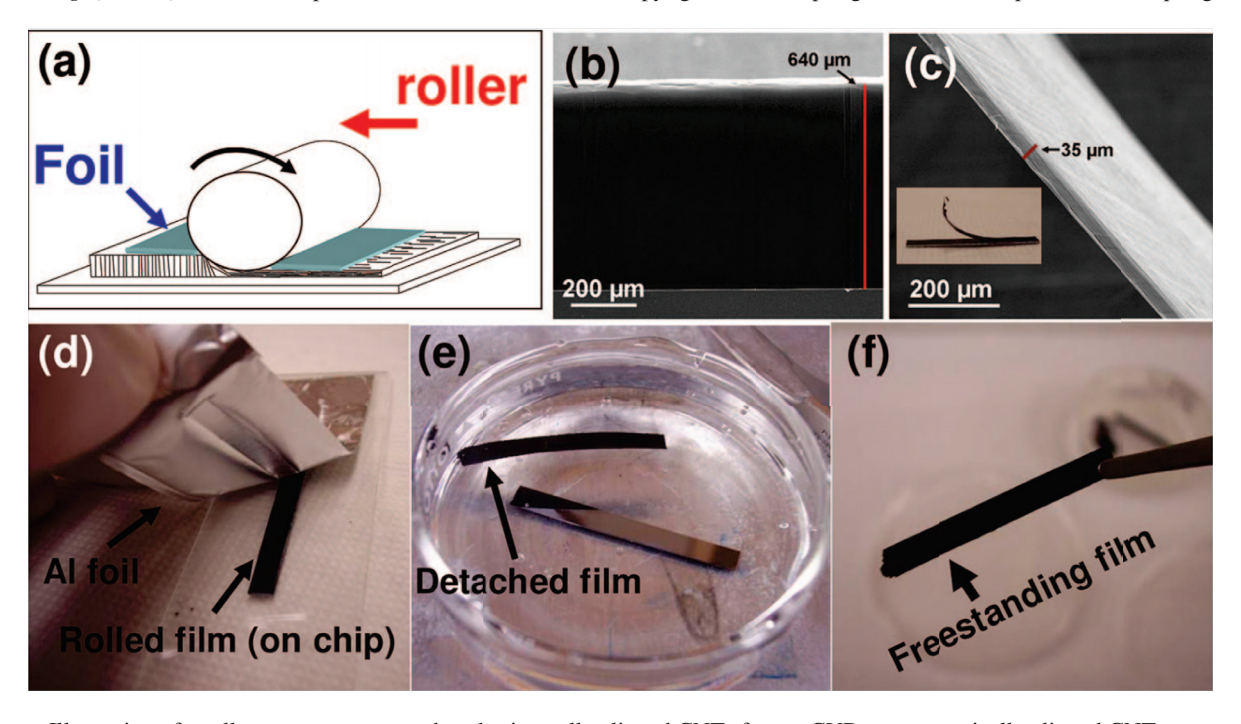


Figure 5. Illustration of a roll-over process to produce horizontally aligned CNTs from a CVD-grown vertically aligned CNT carpet, as well as a method for detaching the CNT film from the substrate. (a) Illustration of the rolling process to form a film of aligned SWCNTs. The film is compressed by applying a downward force while rolling. SEM images of carpets (b) before and (c) after the rolling process. Inset is a photograph of the carpet where the film is peeled. (d) Photograph showing a rolled film as the aluminum foil is removed from the carpet. (e) Detaching films by etching away catalyst in 1 M hydrochloric acid solution to form (f) a freestanding film after being soaked in water. Reprinted with permission from [68]. Copyright © 2008, American Chemical Society.

techniques—chemical vapor deposition (CVD), solution spinning and coating, and controlled vacuum filtration. The first of these is in category (1), whereas the latter two techniques are in category (2).

2.1. Chemical vapor deposition

The CVD growth method can directly produce vertically aligned CNT carpets normal to the growth substrates [64–67]. High catalyst densities cause a crowding effect of the CNTs,

leading to their vertical alignment of CNTs with maximum heights on the order of mm. In order to prepare macroscopic films of horizontally aligned CNTs, the vertically aligned SWCNTs grown using the CVD method can be laid down and be transferred onto any substrates through an easily scalable and dry approach [68]. Figure 5(a) illustrates the rolling-over process developed by Pint *et al* [68] to compress a vertically aligned CNT array grown on a substrate by manually applying downward forces. To keep the carpet from sticking to the roller surface, an aluminum foil was inserted in between. The

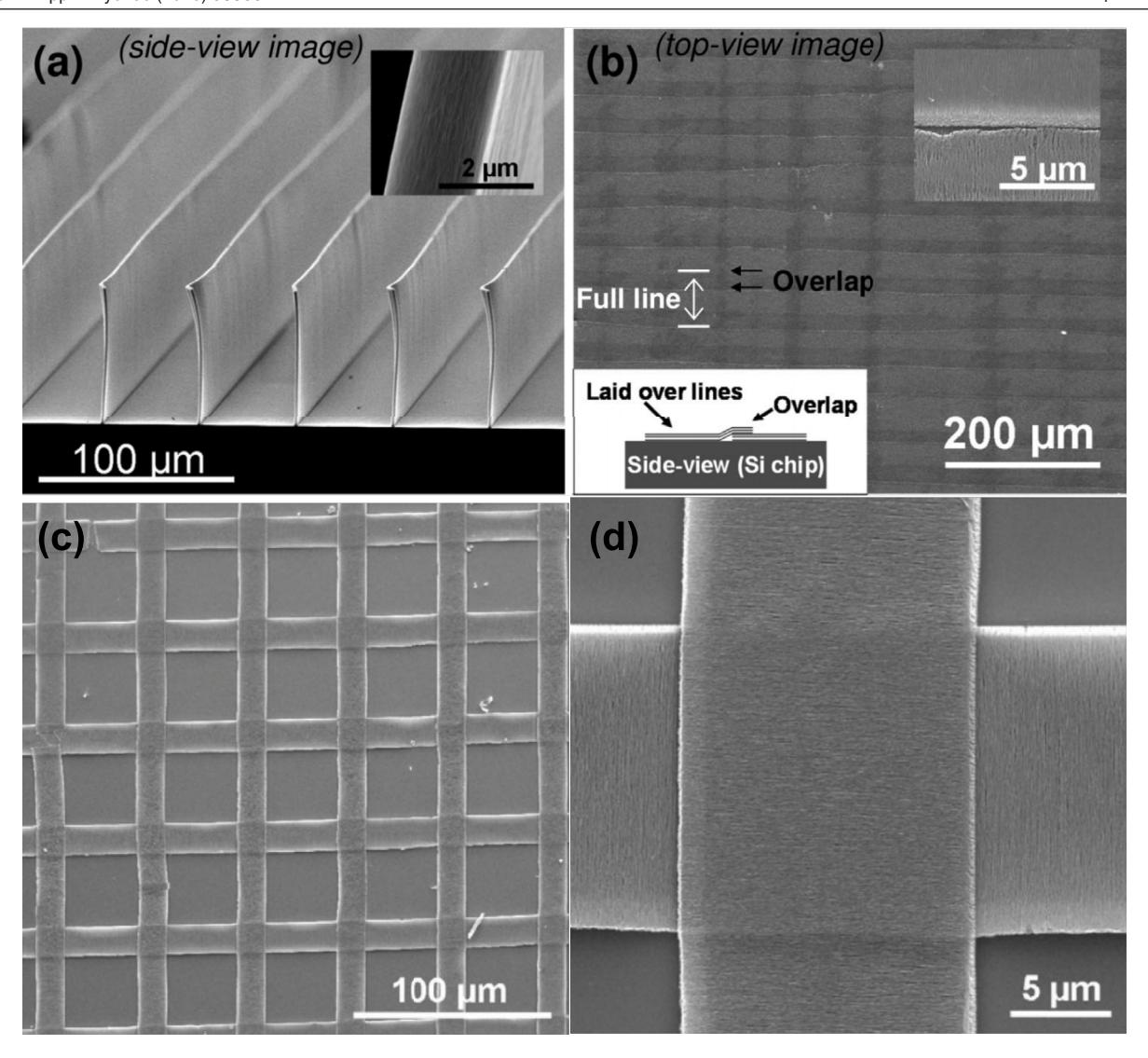


Figure 6. (a) SEM image of vertically aligned SWCNTs with a periodic 50 μ m spacing. Inset is a closer view of the edge of a single line, displaying the aligned SWCNTs inside. (b) Top-view SEM image of the rolled film following the process shown in figure 5. There is an overlap region because the height of obtained films are larger than the period. (c) An SEM image of a grid pattern formed by two transfers, and (d) closer view of the grid pattern showing a single intersection of two individually transferred SWCNT lines. (a), (b) Reprinted with permission from [68]. Copyright © 2008, American Chemical Society. (c), (d) Reprinted with permission from [69]. Copyright © 2010, American Chemical Society.

catalyst-CNT interaction forced the film to remain on the substrate. One crucial point of maintaining the aligned structure, instead of smashing CNTs, is to shear the aluminum foil along the rolling direction. Figures 5(b) and (c) show scanning electron microscopy (SEM) images of carpets before and after the rolling process, respectively. The aluminum foil can be easily detached from CNTs, as shown in figure 5(d). The resulting film can be transferred to other substrates or form a freestanding film, by etching away catalyst using hydrochloride acid (figures 5(e) and (f)).

The horizontally aligned CNT film preserves the alignment in the carpet with a slightly reduced degree of alignment (i.e. nematic order parameter). In order to retain the full carpet alignment after the roll-over process and the ultralong nanotubes achieved through carpet growth in thin films, Pint *et al* [67, 69] utilized photolithography to form thin (2 μ m) lines of catalyst that can be grown to support a 70 μ m-high carpet (figure 6(a)). After the roll-over process described in figure 5,

macroscopically aligned SWCNTs with full surface coverage were obtained despite a small overlap area, as shown in figure 6(b). Moreover, the utilization of photolithography enabled the fabrication of nearly arbitrary patterns of rolled films. Figure 6(c) shows an SEM image at lower magnification of a grid pattern of aligned SWCNTs formed by two orthogonal transfers, while figure 6(d) is an SEM image at higher magnification of the same sample [69].

2.2. CNT-chlorosulfonic acid solution spinning and coating

Superacids such as chorosulfonic acid (CSA) are the only known true solvents for CNTs [70, 71]. Spontaneous dissolution occurs because the strong acid protonates the backbone of the CNT forming a polycarbocation. The repulsive force of the polycarbocations is stronger than the attractive van der Waals forces, resulting in a stable solution of individualized CNTs [70]. Unlike other dispersion techniques such as

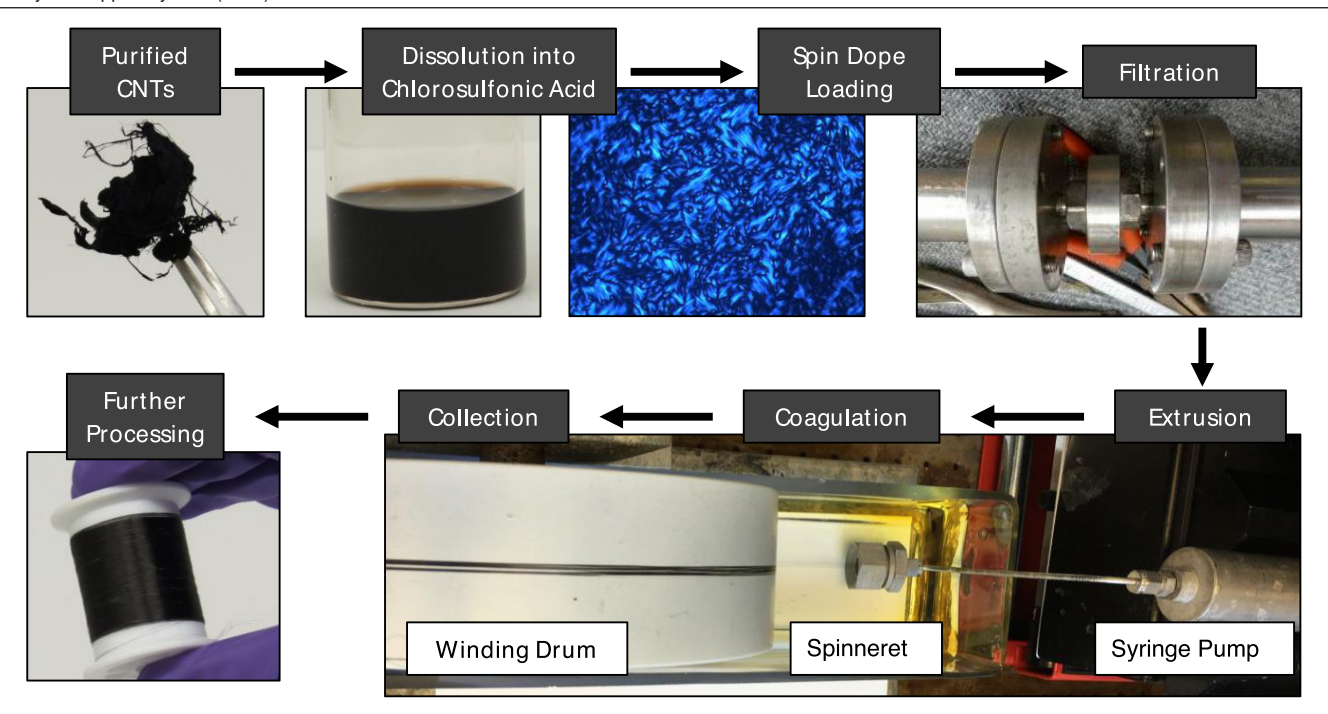


Figure 7. Schematic of the solution spinning process. In brief, CNT solutions are filtered and extruded into a coagulant. The resulting fiber is collected onto a rotating drum. The fiber is stabilized and removed from the drum for further processing. Reprinted with permission from [76]. Copyright © 2017, American Chemical Society.

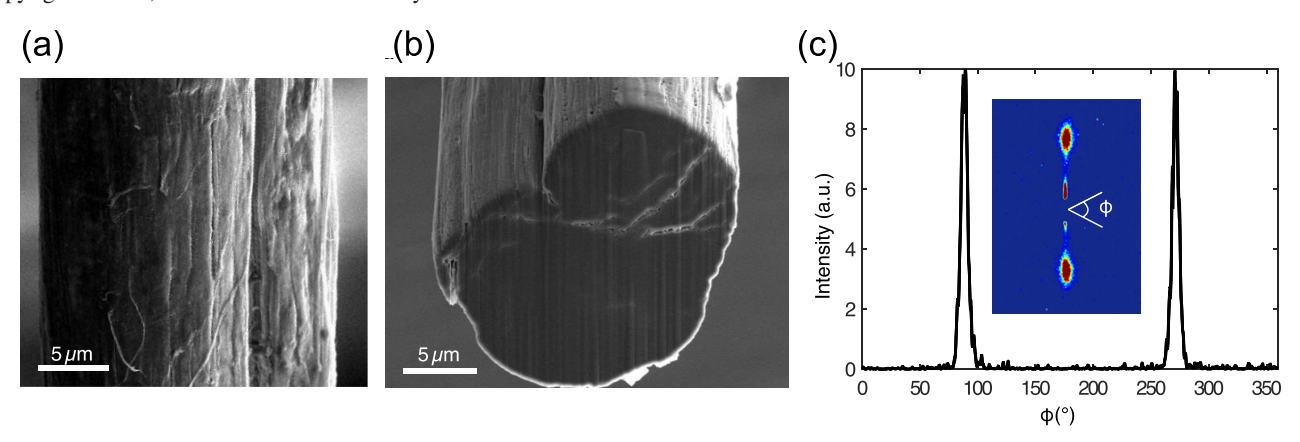


Figure 8. (a) A top-view and (b) a side-view SEM images of solution spun CNT fibers demonstrating the good alignment. (c) X-ray diffraction of a single fiber demonstrating the anisotropic nature. Reprinted with permission from [76]. Copyright © 2017, American Chemical Society.

ultrasonication and chemical functionalization, this method for dispersion does not induce defects in the sp^2 bonding of the CNTs and does not shorten the CNTs [72, 73]. Furthermore, CNTs in CSA behave as expected for rigid rods in solution; at low volume fraction, the solution is isotropic, and with increasing volume fraction, the solution forms liquid crystals [71]. Liquid crystalline solutions can be processed to create highly aligned fibers and coatings.

Continuous lengths of highly aligned CNT fibers can be fabricated using a solution spinning process, similar to the production of Kevlar and Twaron fibers [74–76]. A schematic of the spinning process is demonstrated in figure 7. Purified CNTs are dissolved in CSA at high concentration (1–5 wt%) to create a spin dope. The dope is filtered into a syringe to remove any undissolved particulates. The dope is then extruded through a spinneret into a coagulation bath (typically acetone), and the coagulated fiber is collected onto

a rotating drum. The drum is then washed in water to remove any residual acetone and annealed at 115 °C in an oven overnight to stabilize the conductivity.

The highly aligned fibers obtained through this process is a result of several key processing conditions. Firstly, the CNT dope itself is liquid crystalline, and thus already has domains of aligned CNTs. Secondly, the spinneret suddenly constricts the fluid flow resulting in a high shear that aligns the dope in the flow direction. Lastly, a draw is imposed on the fiber by collecting the fiber on the drum at a faster rate than the extrusion of the dope. This draw further aligns the fiber by applying an extensional flow to the coagulating filament.

The alignment of solution spun fibers can be seen through the SEM images in figures 8(a) and (b). Bundles of CNTs are axially aligned, as expected. Figure 8(c) shows wide angle x-ray diffraction (WAXD) results on a single fiber. The average full width at half maximum (FWHM) was determined to

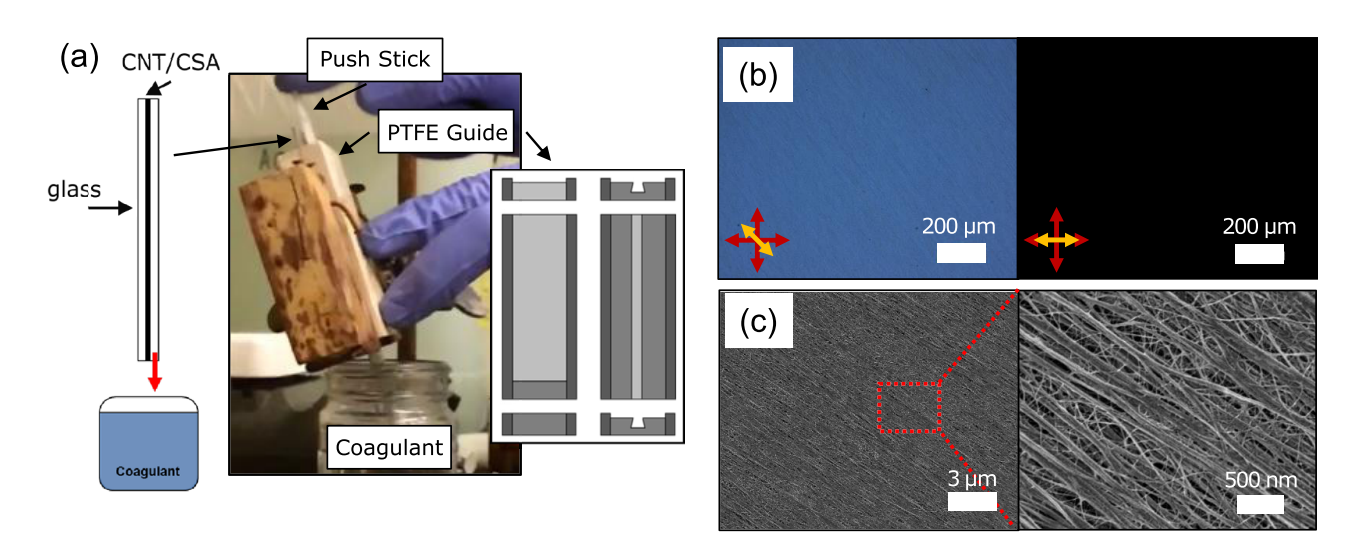


Figure 9. (a) A schematic of the blade coating method demonstrating the solution sandwiched between two slides (left), the PTFE guide holder (right), and the entire apparatus (center). (b) Birefringence from placing a film between a polarizer and a analyzer with the transmission axis 90° rotation (red arrows), when the CNT alignment direction is at 45° and 0° (yellow arrows). (c) SEM images of the coagulated film at low (left) and high (right) magnification. [79] John Wiley & Sons. © 2018 WILEY-VCH Verlag GmbH & Co. KGaA, Weinheim.

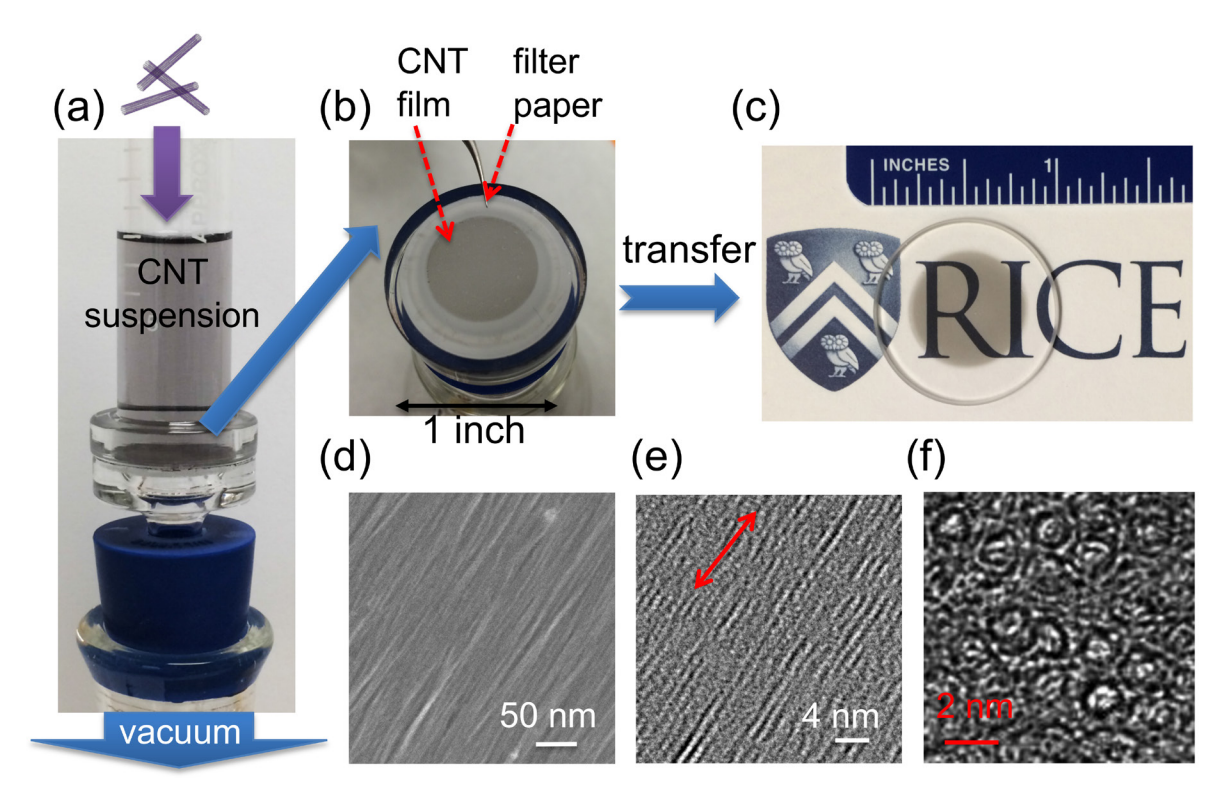


Figure 10. Macroscopically aligned wafer-scale crystalline CNT films made using CVF. (a) A CNT suspension goes through a vacuum filtration system. (b) A 1 inch diameter, uniform CNT film is formed on the filter membrane. (c) Optical image of the produced film after being transferred onto a transparent substrate. (d) A high-resolution SEM image, (e) a topview TEM image, and (g) a cross-sectional TEM image of the film. [80] Copyright © 2016, Springer Nature. With permission of Springer.

be 9.4° [75], corresponding to a 3D nematic order parameter $S_{\rm 3D} = 0.986$, where the value of $S_{\rm 3D}$ ranges from 0 (random distribution) to 1 (perfect alignment) [77, 78]. Due to the use of pristine CNTs and the alignment obtained with this method, the fibers have outstanding properties. To date, the highest conductivity achieved with this method is 8.5 MS/m, and the highest tensile strength is 2.4 GPa [76].

Thin films and short fibers (~7 cm) of aligned CNTs can also be produced using a facile blade coating technique [79]. This process begins with 0.5 wt%–2 wt% solutions of CNTs in CSA. The solution is pipetted onto a glass microscope slide and pressed between another slide to fully coat both slides, as shown in figure 9(a). The slides sandwiched with solution are put into a custom-built poly(tetrafluoroethylene) (PTFE) holder. A PTFE

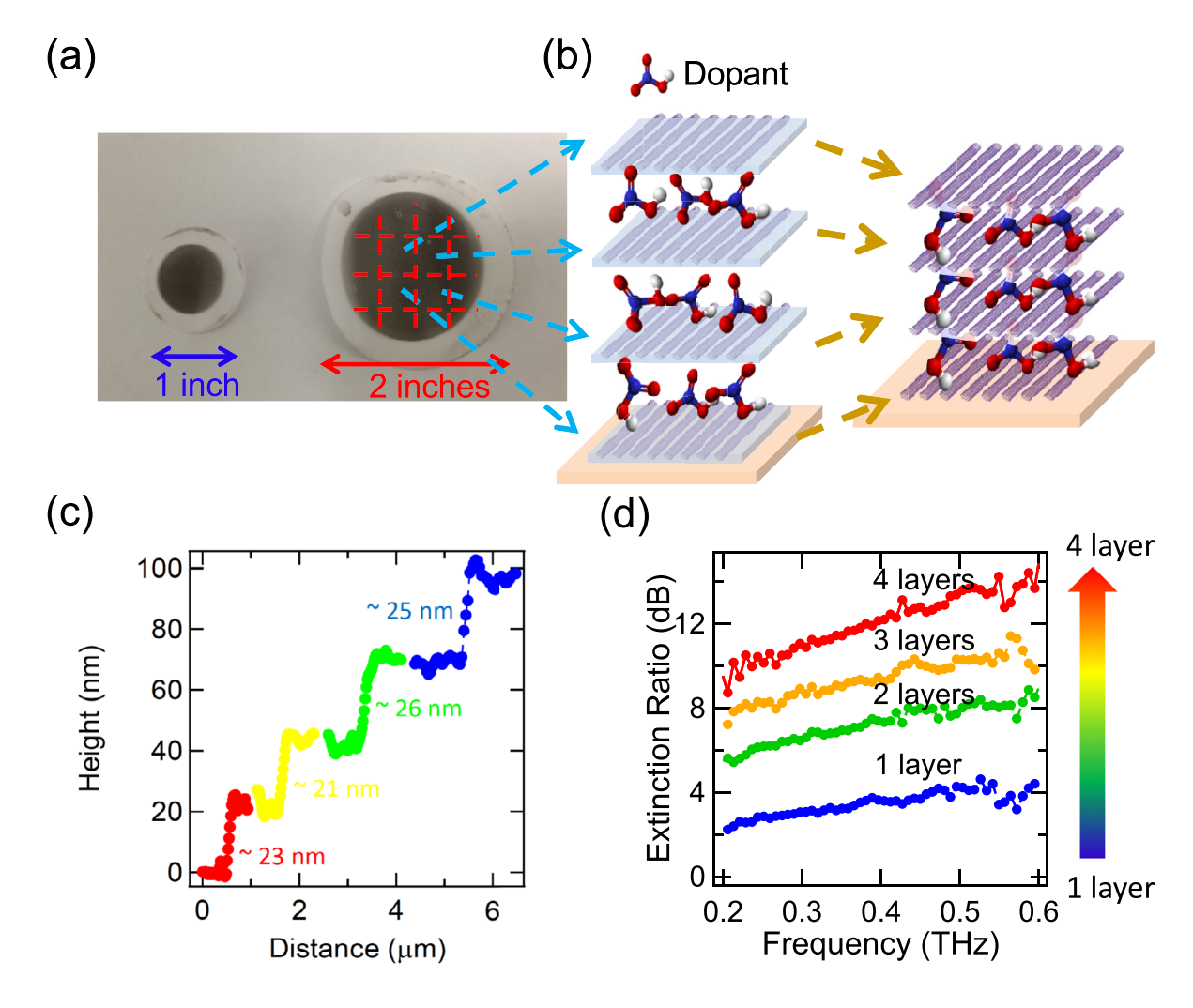


Figure 11. Scalability of films obtained through CVF. (a) One 1-inch-diameter SWCNT film and one 2-inch-diameter SWCNT film produced on filter membrane. (b) Illustration of 3D CNT architecture from layer stacking and dopant molecule intercalation. (c) Height profile of 3D CNT architecture consisting of one to four constitute layers. (d) Extinction ratio of aligned SWCNT films for THz radiation for one to four constitute layers. [82] John Wiley & Sons. © 2017 WILEY-VCH Verlag GmbH & Co. KGaA, Weinheim.

push stick is used to quickly shear (at a rate of $\sim 10^4 \, s^{-1}$) the two glass sides apart from each other. This shearing force induces a uniaxial alignment of the CNTs. The films are then slowly coagulated to remove the CSA and stabilize the aligned films.

The large-scale alignment of the films is demonstrated through polarized optical microscopy in figure 9(b). When the film is rotated 45° from the polarizer and analyzer directions (red arrows), the light is rotated and allowed to pass through. However, when the film is rotated to be parallel to the incident light, the birefringent image disappears. Furthermore, the alignment of the CNTs is seen visually via SEM images in figure 9(c). Using WAXD, the films were determined to have an average FWHM of 15.2°, corresponding to $S_{3D} = 0.974$. These films can be used for various electronic applications without further processing, or small sections of the film can be peeled off and twisted into a short fiber. The resulting fibers, although slightly more disordered, demonstrate similar electrical conductivity, but higher tensile strength when compared to solution spun fibers made with the same aspect ratio. The

increase in tensile strength is attributed to improved packing density of the short fibers.

2.3. Controlled vacuum filtration

Recently, He and coworkers have developed a novel technique for making macroscopically aligned films from a solution of dispersed SWCNTs using controlled vacuum filtration (CVF) [80, 81]. This technique yields uniform and monodomain SWCNT films with an extremely high degree of alignment (2D nematic order parameter $S_{\rm 2D}\approx 1$), high packing density (3.8 × 10⁵ tubes in a cross-sectional area of 1 μ m²), large areas (~2 inches in diameter) and controlled thickness (between a few nm and ~100 nm). Furthermore, CVF is simple, reproducible, and effective for all SWCNTs, regardless of their synthesis method, band structure, or chirality. Given that these films are compatible with standard micro/nanofabrication techniques, their exciting applications in electronic and photonic devices are realizable.

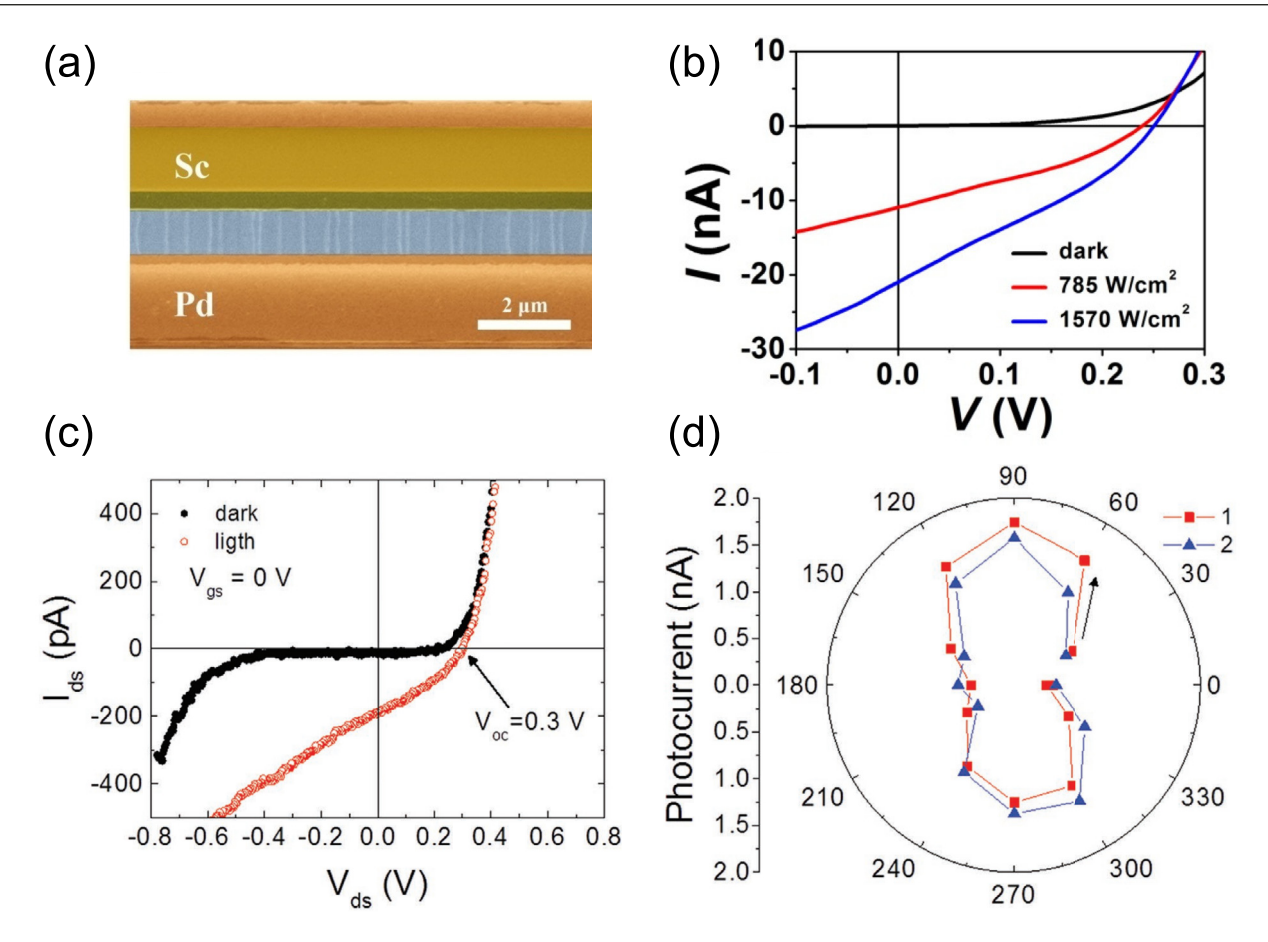


Figure 12. (a) SEM image of a barrier free bipolar diode photodiode consisting of a SWCNT array. (b) Current-voltage (I-V) characteristics of the detector, in the dark and under illumination with a power density of 785 and 1570W cm⁻². (c) I-V characteristics of a detector in the dark and under illumination with a wavelength of 1.55 μ m. The detector is based on a SWCNT array with Sc-Pt asymmetric contacts. (d) Polarization sensitivity at a wavelength of \simeq 1.55 μ m. Two consecutive 360 degrees measurements at zero bias with polarized light. The vertical direction is the drain-to-source direction. (a), (b) Reproduced with permission from [90]. © 2012 Optical Society of America. (c), (d) [91] John Wiley & Sons. © 2017 WILEY-VCH Verlag GmbH & Co. KGaA, Weinheim.

The CVF process begins with a dispersion of individual CNTs stabilized by surfactants to prevent bundling. The CNT suspension is then held above a filter membrane with a pore size smaller than the CNT length; see figure 10(a). A differential pressure applied across the membrane by a vacuum pump causes water and surfactant molecules to pass through the membrane while CNT passage is blocked; see figure 10(b). The resulting CNT film can be removed from the membrane by dissolving the membrane in organic solvents. Figure 10(c) shows a film transferred onto a quartz wafer.

Although vacuum filtration has been widely recognized as a method of producing only films of randomly oriented CNTs [37], He *et al* empirically found that achieving well-aligned films require the following three conditions: (1) the surfactant concentration must be below the critical micelle concentration. (2) The CNT concentration must be below a threshold value. (3) The filtration process must be slow. It was also found that the filter membrane's surface and CNTs' structural parameters impact the optimal conditions for macroscopic alignment. The SEM image in figure 10(d) and the transmission electron microscopy (TEM) image in figure 10(e) show

aligned SWCNTs, and the cross-sectional TEM image in figure 10(f) shows a highly packed structure.

Obtained films can scale up laterally, and one can stack multiple films while intercalating external molecules in between to form doping-engineered 3D CNT architectures, as demonstrated by Komatsu et al [82]. The lateral size is limited by the size of the CVF system and thus, CVF systems that can support 2-inch diameter filter membranes vield larger films; see figure 11(a). Figure 11(b) illustrates how these largerarea films can be used to construct more exotic 3D SWCNT architectures through layer stacking and molecule intercalation. Fabricating these architectures requires manually stacking single sheets of aligned SWCNT films with precise control over their relative angles, and n-type or p-type doping can be achieved by doping electron donors or acceptors, respectively [82]. These films are compatible with diverse dopants, such as HNO₃ [83], H₂SO₄ [83, 84], NH₄S₂O₈ [84], HCl [83], H₂SO₃ [85], iodine solution [85], and benzyl vilogen [86]. Figure 11(c) displays AFM measurements for the height profile of a produced multilayer structure consisting of four stacked aligned CNT films, illustrating that this method

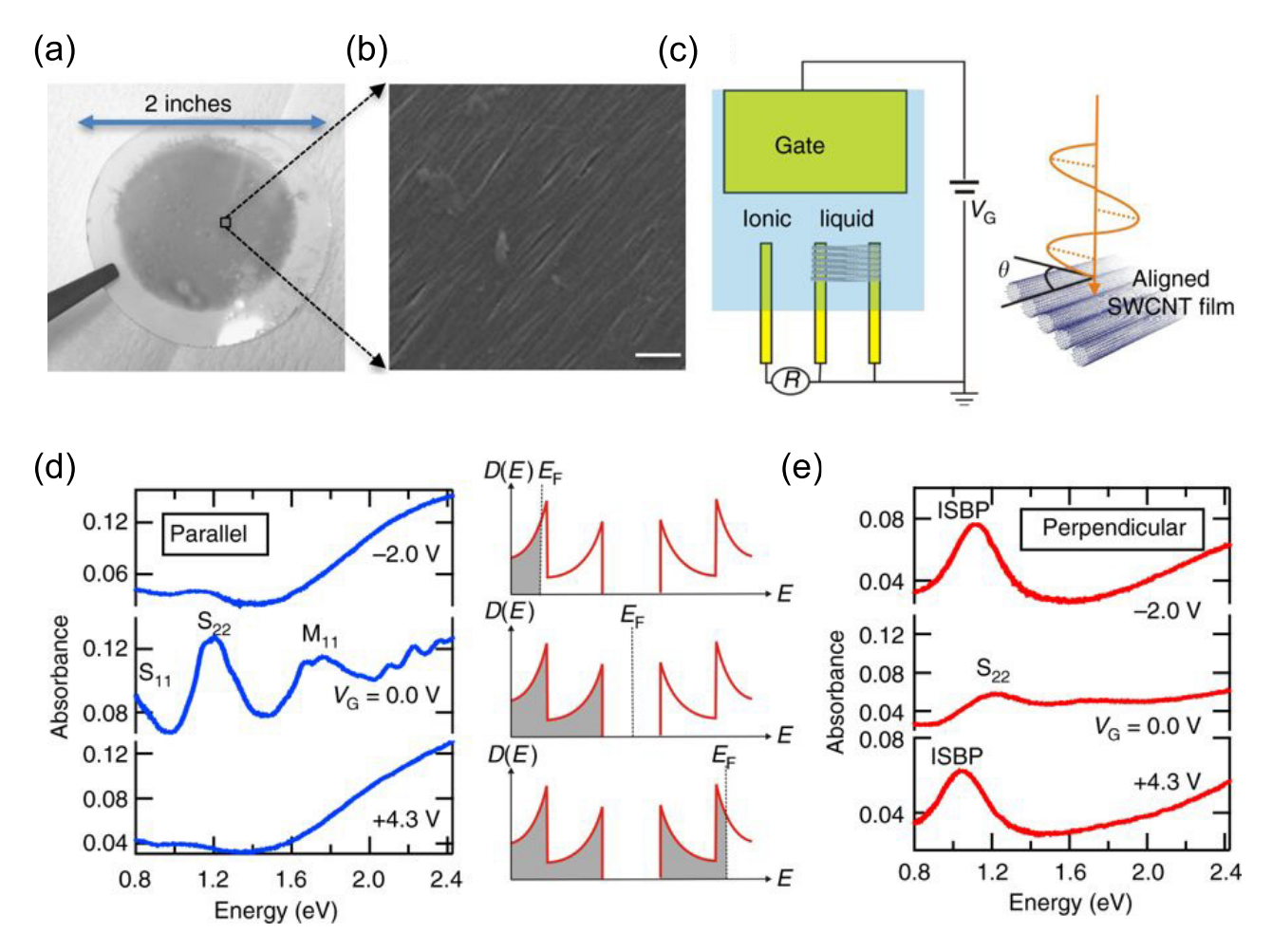


Figure 13. ISBP peak in aligned and gated SWCNT films. (a) Optical and (b) SEM images of a film of aligned SWCNTs. The scale bar is $100 \, \text{nm}$. (c) Schematic images of the experiments. The Fermi level of an aligned SWCNT film was varied through electrolyte gating. The probe light polarization was rotated by angle θ with respect to the CNT alignment direction. V_G : gate voltage, R: reference voltage. (d), (e) Absorption spectra with different gate voltages for (d) parallel polarization and (e) perpendicular polarization. The ISBP peak appears only for perpendicular polarization and only when carriers are present either in the valence band or the conduction band, corresponding to $V_G = -2.0$ and $4.3 \, \text{V}$, respectively. Reproduced from [97]. CC BY 4.0.

can yield reproducible structures with well-controlled geometries. The extinction ratio between the parallel and perpendicular polarizations for THz radiation increases essentially linearly with the film thickness, as shown in figure 11(d), indicating that alignment is well preserved during the stacking process.

3. Flexible devices based on macroscopically aligned CNTs

3.1. Flexible photodetectors

The rapid development of soft and mobile electronics and optoelectronics in recent years demands new types of photodetector materials with flexibility, reduced weight, and high absorption coefficients. CNTs possess all these characteristics necessary for developing flexible photodetectors. In addition, fabrication processes for CNT-based devices are compatible/adaptable with conventional silicon processing technologies. Furthermore, a CNT ensemble with mixed chiralities can absorb light in an ultrabroad wavelength range, from the THz

to the ultraviolet, while a single-chirality CNT ensemble can provide tunability by selecting the chirality with an absorption peak at the desired wavelength [10]; see recent reviews of carbon-based photodetectors [87–89]. Below, we focus on recent work utilizing aligned CNTs.

Among different types of photonic detectors based on CNTs, photodiodes have been intensively studied. In a photodiode, photocurrent is generated when a built-in electric field separates optically excited electron-hole pairs into free carriers. For example, a barrier free bipolar diode can utilize asymmetric contacts, such as Pd and Sc or Y [92, 93], forming an ohmic contact between the valence band of the SWCNT and Pd, and between the conduction band of the SWCNT and Sc or Y. This induces band bending across the channel, leading to electron-hole separation

Zeng *et al* implemented this approach to films of random [94] and aligned [90] SWCNTs; see figure 12(a). They used semiconductor-enriched SWCNTs because metallic SWCNTs lower the detector response speed and sensitivity [88, 95]. Figure 12(b) demonstrates photocurrent generation under illumination due to electron-hole separation by a built-in electric

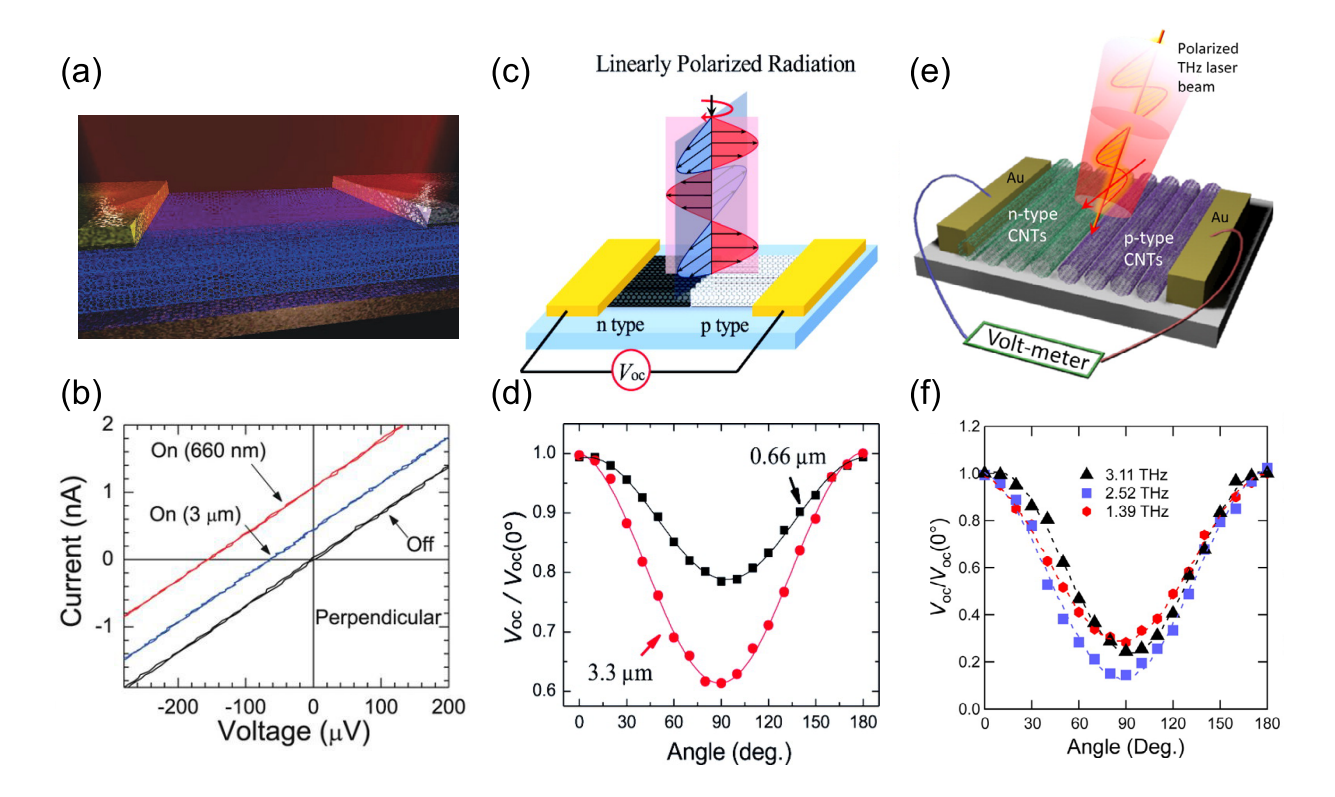


Figure 14. (a) A schematic image of a photothermopile based on an aligned CNT film with Ti and Pd contacts. (b) *I-V* characteristics of a device in which current flows in a direction perpendicular to the CNT alignment direction under illumination by light with a wavelength of 660 nm and 3 μ m. (c) A schematic image of a CNT photothermopile based on a p-n junction under illumination by polarized light. (d) Polarization dependence of the photovoltages obtained at 660 and 3300 nm, respectively. (e) A schematic image of a CNT THz detector under illumination by polarized THz radiation. (f) Polarization dependence of photovoltage at different THz frequencies. (a), (b) [102] Copyright © 2013, Springer Nature. With permission of Springer. (c), (d) Reprinted with permission from [103]. Copyright © 2013, American Chemical Society. (e), (f) Reprinted with permission from [86]. Copyright © 2014, American Chemical Society.

field. Alignment minimizes the number of intertube junctions, which allows excitons to diffuse along the SWCNT channel to the electrodes more easily [88], improving the on/off ratio of the device and minimizing screening effects [91]. The responsivity of their photodiode under infrared (IR) illumination was estimated to be 6.58×10^{-2} A W⁻¹, based on the actual area of CNTs.

Balestrieri *et al* used the same approach and fabricated a novel photodiode. This device operated not only in the IR range but also in the telecom wavelength range [91]; see figure 12(c). Furthermore, the aligned CNT structure provided a unique and useful feature—polarization sensitivity. Figure 12(d) shows that the intensity of photocurrent depends on the incident light polarization; a maximum photocurrent was obtained for light polarized parallel to the SWCNT axis, and it was five times larger than the perpendicular polarization.

While the examples above are based on interband absorption, intersubband absorption can also be utilized as in quantum-well IR photodetectors [96]. Recently, Yanagi *et al* observed a near-IR intersubband plasmon (ISBP) peak in aligned and gated SWCNT films [97]. They used the CVF method (see section 2.3) to fabricate macroscopically aligned SWCNT films, as shown in figures 13(a) and (b) [80]. To observe the ISBP, the probe light polarization has to be perpendicular to the CNT axis and the film has to be gated sufficiently strongly to have carriers either in the conduction band or the valence

band (figures 13(c)–(e)). Previous studies revealed a new absorption band in heavily doped SWCNT samples [98–101], but the interpretation of its origin was challenging because the SWCNTs were randomly oriented. Furthermore, the 1D nature of aligned CNTs allows their ISBPs to be excited with normal incidence light unlike quantum wells, simplifying the experimental geometries. Applications of ISBPs in aligned SWCNTs such as photodetectors and quantum cascade lasers will have great potential.

A photothermopile is a thermal-based photodetector using the photothermoelectric (PTE) effect [88]. Photoabsorption creates a temperature gradient, which generates a voltage through the Seebeck effect. One of the advantages of CNT-based thermopiles is their ultrabroadband response arising from the ability of CNTs to absorb electromagnetic radiation from the ultraviolet to the THz. Nanot *et al* [102] reported a photothermopile based on an aligned CNT film prepared by the CVD method (see section 2.1). In this work, vertically aligned SWCNTs were dry transferred onto a substrate to form a horizontally aligned SWCNT film. Asymmetric electrodes (Pd and Ti) were made at two ends of the film, as schematically shown in figure 14(a), and they observed photocurrent in the IR range (0.66–3.15 μ m); see figure 14(b).

He *et al* proposed a CNT photothermopile based on an in-plane p-n junction to improve the sensitivity (figure 14(c)) [103]. The CNT thin film was made by transferring

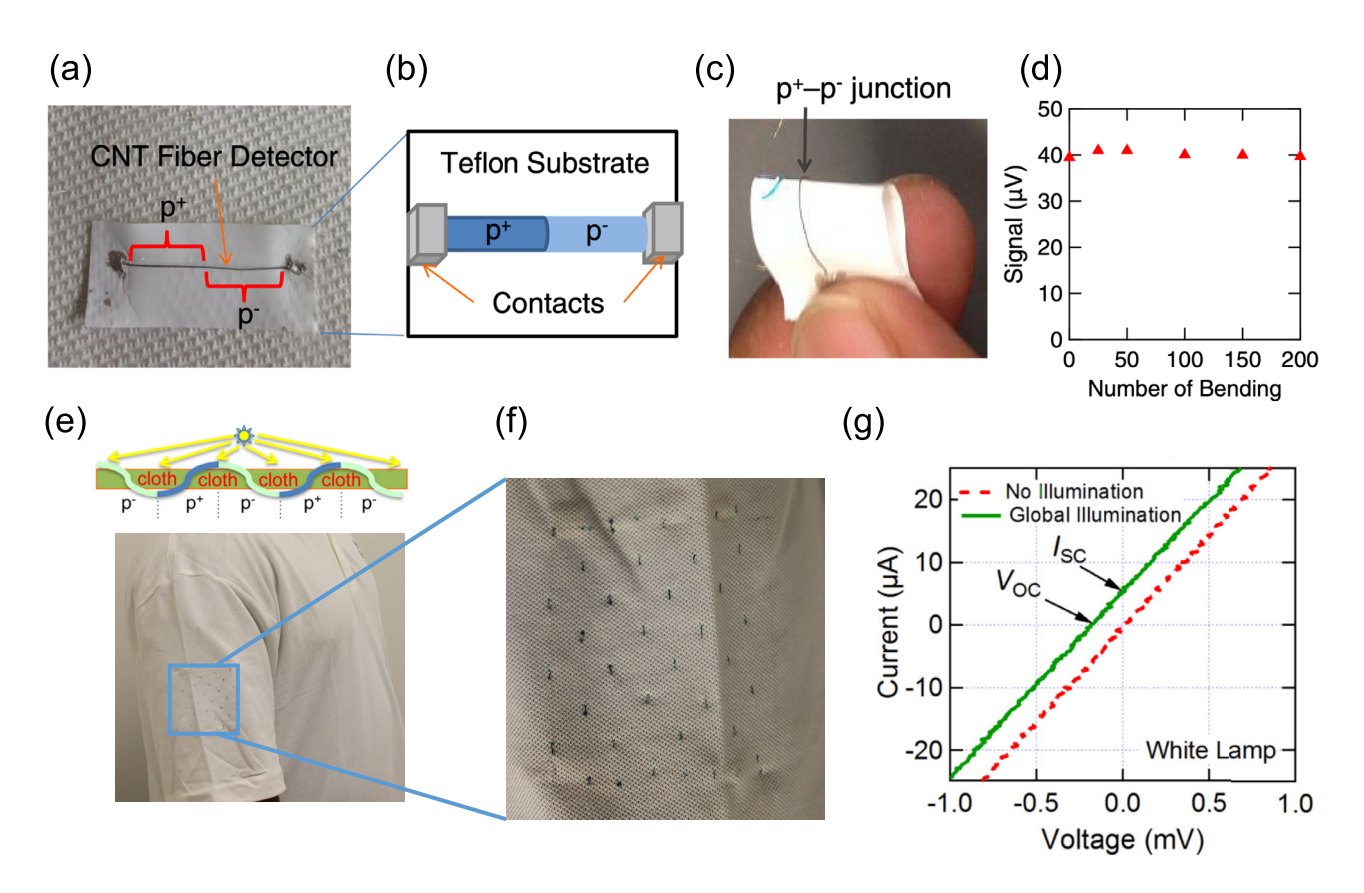


Figure 15. (a) Optical and (b) schematic images of a flexible CNT fiber detector with a $p^+ - p^-$ junction on a Teflon substrate. (c) The detector can be bent, and (d) photovoltage does not degrade even after 200 bending cycles. (e) CNT detector sewn into a shirt, in such a way that the $p^+ - p^-$ junctions are under illumination while the $p^- - p^+$ junctions are inside the shirt (inset). (f) The front side of the shirt, with $p^+ - p^-$ junctions exposed to illumination. (g) *I-V* characteristics of the detector in dark and under global illumination by a white lamp. Reprinted figure with permission from [105], Copyright © 2018 by the American Physical Society.

a CVD-grown vertical array of aligned SWCNTs (see section 2.1). To create an in-plane p-n junction, they chemically doped a half of the initially p-type film with benzyl viologen (BV), which is an n-type dopant for CNTs. This device based on aligned CNTs with a p-n junction showed polarization sensitivity (figure 14(d)); it also extended the operation wavelength to the mid-IR with sustained efficiency. He $et\ al$ further developed a CNT p-n junction thermopile that works in the THz region [86]. Their detector was demonstrated to be sensitive at frequencies from 1 to 3 THz, with a maximum responsivity of $\sim 2.5 \text{ V W}^{-1}$ and a maximum polarization ratio of $\sim 5:1$ (figures 16(e) and (f)). The device also worked on a flexible Teflon substrate.

Most recently, Zubair *et al* developed flexible CNT fiber photodetectors based on the PTE effect [104]. The CNT-CSA solution spinning method (section 2.2) was used to fabricate the fibers, consisting of aligned and packed CNTs. By making the initially heavily doped fiber (p^+ -doped fiber) less p doped (p^- -doped fiber) by partially removing the dopants through current annealing, a $p^+ - p^-$ junction was formed. Figures 15(a) and (b) show images of the CNT fiber detector with a $p^+ - p^-$ junction. This detector worked in an ultrabroad range (ultraviolet to THz), with an optimal responsivity of 0.33 V W⁻¹ at 96.5 μ m, and exhibited polarization sensitivity. It was highly flexible as shown in figure 15(c), and its

performance did not degrade after 200 cycles of bending (figure 15(d)). Finally, the fiber detector were woven into textiles (figures 15(e) and (f)), generating a photovoltage under illumination by white light (figure 15(g)).

We summarize the performance of discussed photodetectors in table 1 and strain sensors in table 2.

3.2. Flexible strain sensors

The emergence of the field of wearable biomedical device development has created a great demand for soft electronic devices [110–114]. In particular, flexible strain sensors are vital for human motion detection, and thus, various types of sensing materials and structures have been extensively investigated [115–117]. Sensitivity, stretchability, and stability are the three important parameters assessing the performance of flexible strain sensors. Conventional metal gauges possess high sensitivity, but their stretchability is low. CNTs have been extensively studied for strain sensor device applications because of their excellent mechanical properties and high electrical conductivity.

Individual CNTs exhibit high elasticity and very high sensitivity [118–123], making them promising materials for strain sensors. The sensitivity is assessed by the gauge factor GF, which is defined as $GF \equiv (\Delta R/R)/\epsilon$, where R is the

Table 1. Summary of photodetectors based on aligned CNTs.

		, ,		\mathcal{C}		
Material	Alignment	Density	Wavelength	Maximum responsivity	Architecture	Mechanism
Semiconductor-enriched CVD SWCNTs [90]	Horizontally aligned CNTs	Low	785 nm	$6.58 \times 10^{-2} \text{ A}$ W^{-1}	Barrier free bipolar diode (BFBD)	Photovoltaic
Semiconductor-enriched laser-ablation SWCNTs [91]	Dielectrophoresis	Low	$1.25 – 1.68 \mu\mathrm{m}$	Not reported	BFBD	Photovoltaic
Unsorted CVD SWCNTs [102]	Rolling over vertically aligned CNTs	High	660 nm and 1.35–3.15 μ m	$28~\mathrm{mV}~\mathrm{W}^{-1}$	Asymmetric electrodes	Photothermoelectric
Unsorted CVD SWCNTs [103]	Rolling over vertically aligned CNTs	High	$660\mathrm{nm}$ to $3.3~\mu\mathrm{m}$	$1\mathrm{V}\mathrm{W}^{-1}$	p-n junction	Photothermoelectric
Unsorted CVD SWCNTs [86]	Rolling over vertically aligned CNTs	High	96.4–215.7 $\mu \mathrm{m}$	$2.5 V W^{-1}$	p-n junction	Photothermoelectric
Unsorted CNT fibers [104]	Spinning CNT-CSA solution	High	405 nm–215.8 μ m	$0.33 \text{V} \text{W}^{-1}$	p ⁺ -p ⁻ junction	Photothermoelectric

Table 2. Summary of strain sensors based on aligned unsorted CNTs.

Architecture	Alignment	Density	Alignment to strain	Gauge factor	Stretchability	Stability
CVD SWCNTs on PDMS [105]	Removing films from vertically aligned CNTs	High	Perpendicular	0.82 (0%–40%), 0.06 (60%–200%)	280%	10 000 cycles at 150% strain, 3300 cycles at 200%
CVD CNTs on PDMS [106]	Drawing films from vertically aligned CNTs	High	Perpendicular	0.12 (0%–100%), 0.075 (100%–300%), 0.2 (300%–400%)	400%	5000 cycles at 400%
CVD CNT yarns in epoxy resin [107]	Spinning fibers from vertically aligned CNTs	High	Parallel	0.38	3.5%	Not reported
CVD CNT fibers on elastic substrates [108]	Spinning fibers from vertically aligned CNTs	High	Parallel	0.56 (0%–200%), 47 (200%–440%)	440%	
[]				Prestrain: 0.54 (0%–400%), 64 (400%–960%)	960% (prestrain)	10 000 cycles at 300%
SWCNTs sandwiched between PDMS [109]	Blade coating CNT-CSA solution	High	Perpendicular	1	50%	60 cycles at 50%
SWCNTs sandwiched between PDMS [109]	Blade coating CNT–CSA solution	High	Parallel	59	16%	60 cycles at 16%

resistance and ϵ is the applied strain. The effective piezore-sistive gauge factor of an individual CNT is as high as 2900 [122]. Early studies on CNT flexible strain sensors utilized buckypapers [124–126]. They showed a relatively high GF of over 3, which is close to the GF of conventional foil strain gauges [126]. However, they showed low stretchability and stability. Furthermore, they did not have any direction sensing ability due to the isotropic nature of buckypaper [124–126].

Flexible strain sensors using networks of aligned CNTs resulted in higher stretchability and better stability compared to random networks of CNTs [105–109, 127, 128]. Yamada *et al* prepared a film of aligned SWCNTs from vertically aligned SWCNTs by water-assisted CVD [66] on a polydimethylsiloxane

(PDMS) substrate [105], as schematically shown in figure 16(a). The CNT alignment direction was perpendicular to the strain axis. The resistance of the film monotonically increased up to 280% strain, much higher than the stretchability of conventional metal strain gauges (\sim 5%) or that of a film of randomly oriented SWCNTs (figure 16(b)). The *GF* was calculated to be 0.82 (0%– \sim 40% strain) and 0.06 (\sim 60%–200%). The sensor was stable for 10000 cycles at 100% and 150% strain, \sim 3300 cycles for 200% strain (figure 16(c)). Yu *et al* designed a flexible and transparent strain sensor by using aligned CNTs [129, 130] films on PDMS substrates [106], with the alignment direction perpendicular to the strain axis. Their sensor also showed a monotonic and fully reversible change in resistance up to as high as 400%.

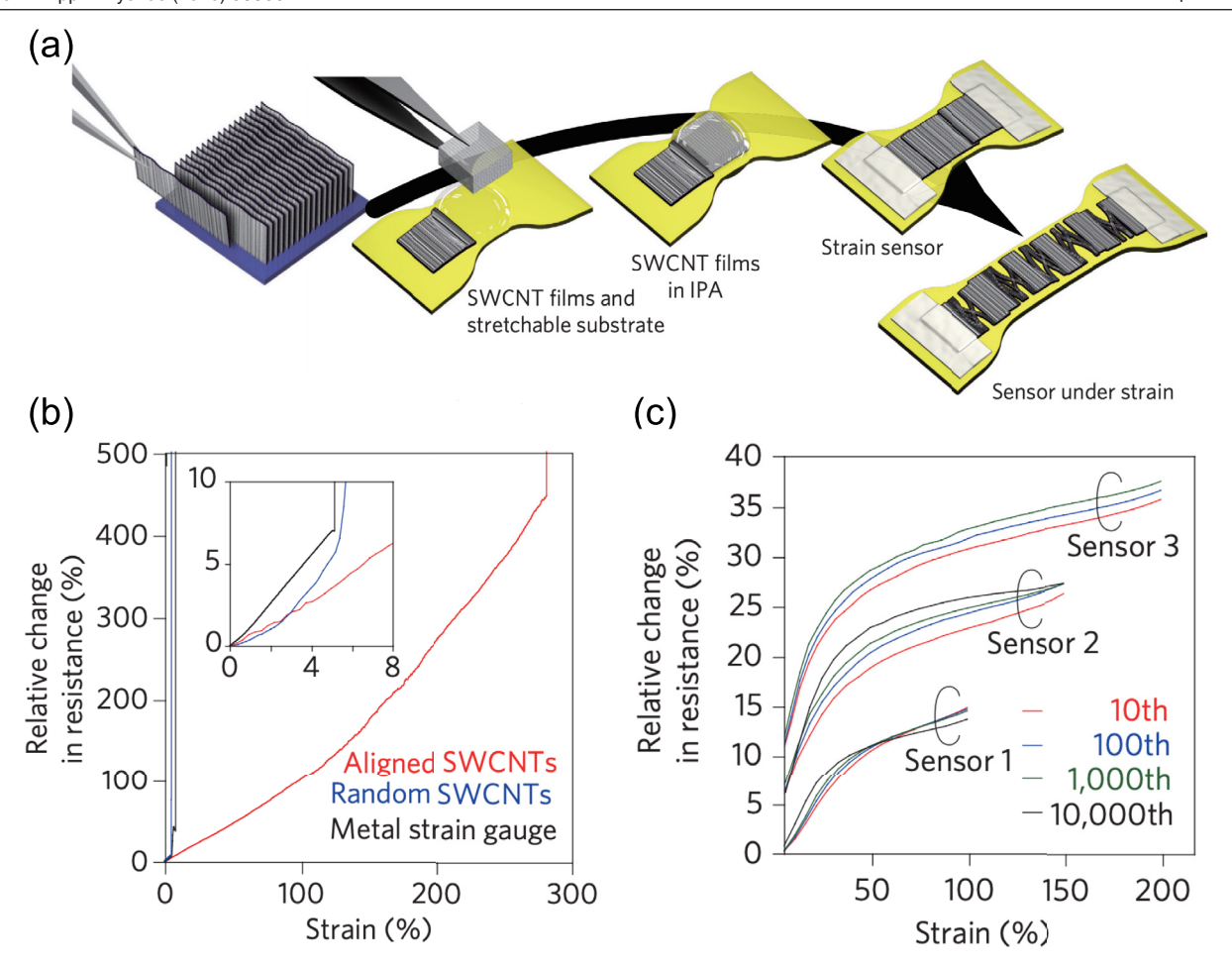


Figure 16. Strain sensor made of aligned SWCNT films. (a) Vertically aligned SWCNT film was transferred onto a PDMS substrate. (b) Relative change of resistance due to applied strain in films of aligned SWCNTs (red), random SWCNTs (blue), and metal strain gauge (black). Inset: zoom-in of the low strain region. (c) Relative change of resistance due to applied strain of multiple cycles, demonstrating the stability: after the 10th (red), 100th (blue), 1000th (green), and 10 000th cycle (black). Sensors 2 and 3 are intentionally offset by 5% and 10%, respectively. [105] Copyright © 2011, Springer Nature. With permission of Springer.

Zhao *et al* used CNT yarns directly as piezoresistive strain sensors [107]. A CNT array was grown by CVD [131]. CNT ribbons were pulled out from the array and then spun to form a CNT yarn. The resistance change of the yarn showed a linear relationship with the longitudinal strain up to 3.5%, and the *GF* was 0.38 [107]. Ryu *et al* used CNT fibers produced by a dry-spinning process [129] to create a highly oriented CNT array [108]. An aligned fiber was attached directly to an elastic substrate with the CNT alignment direction parallel to the strain axis. With the support of the substrate, the stretchability of the sensor was enhanced to 440%. The authors further improved the stretchability by introducing a preliminary strain in the substrate, and the stretchability reached 960%. The *GF* was calculated to be 0.54 (0%–400% strain) and 64 (400%–960%).

Sui *et al* studied an aligned SWCNT film under strain applied in the parallel (\parallel) and perpendicular (\perp) directions to the alignment direction and found significant anisotropy in sensitivity and stretchability [109]. They attributed this anisotropy to different deformation mechanisms in the different

directions. The aligned SWCNT film was prepared by a facile blade coating technique [79] (see section 2.2) and was sandwiched between two PDMS layers (figure 17(a)). Figure 17(b) shows anisotropy in electrical response to an applied strain; the resistance stably increases until 16% (50%) along the (\perp) direction and then increases dramatically. Figures 17(c) and (d) demonstrate that the resistance change is higher and stretchability is lower for the || case, while the resistance change is lower and stretchability is higher for the \perp case. The authors conducted an in situ tensile test as well as a coarsegrained molecular dynamics simulation, and found that the shear force dominates the interface with the strain along the direction, while the contact areas were preserved by SWCNT bridges linking the gaps along the \perp direction (figure 17(e)). The GF along the \parallel direction was 59 at a strain of 0%–16%, while it was 1 along the \perp direction at a strain of 0%–50%. The authors further demonstrated a direction-sensitive strain sensor consisting of a cross-like laminated structure composed of two aligned SWCNT films, taking advantage of the anisotropic nature of their sensors (figure 18).

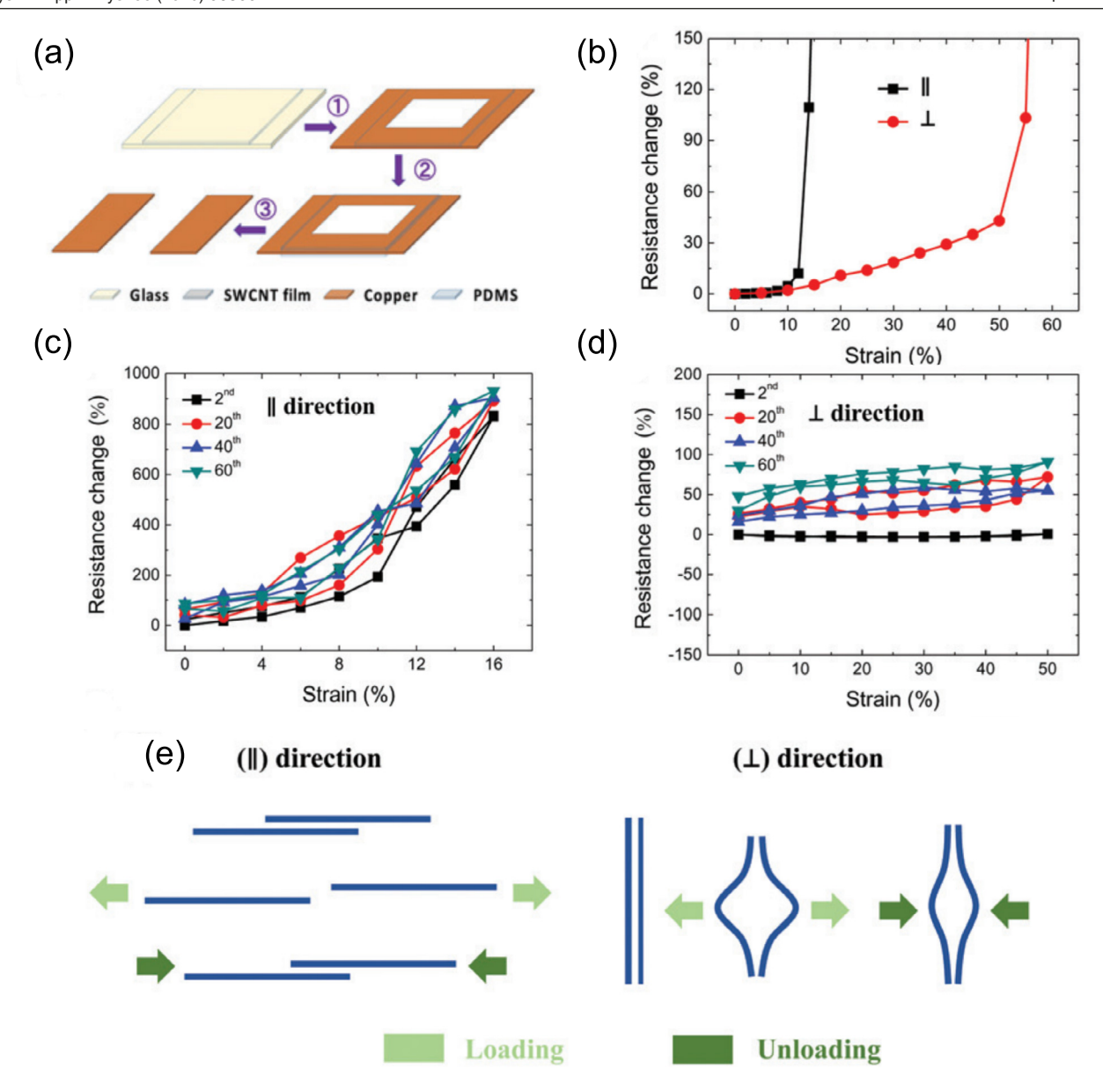


Figure 17. Studies of an aligned SWCNT film under applied strain. (a) Schematic for preparing a SWCNT film composite. The SWCNT film was suspended over a hole in a copper sheet. (b) Relative change in resistance under initial tensile loading applied along the \parallel direction (black) and the \perp direction (red). (c), (d) Relative change in resistance under strain applied along the \parallel and \perp directions for multiple cycles, demonstrating the stability. The 2nd (black), 20th (red), 40th (blue), and 60th cycle (green). (e) Schematic for deformation mechanism of SWCNTs under a strain applied along the \parallel and \perp directions. Reproduced from [109] with permission of The Royal Society of Chemistry.

4. High-temperature devices based on macroscopically aligned CNTs

4.1. Thermal emitters

Thermal emitters are optical devices that convert heat to thermal radiation. They can become novel light sources for applications such as sensing as well as waste heat recovery through thermophotovoltaics (TPV) [132, 133]. The high temperature stability, up to 1600 °C, and unique optical properties make CNTs an exciting low-dimensional material platform for designing new thermal emitters [80, 134, 135].

The ultrastable chemical structure of CNTs motivated early studies of black-body emission from current-heated filaments made of macroscopic ensembles of SWCNTs and MWCNTs [136–140]. One design goal of thermal emitters is to have an emissivity near unity. Vertically aligned films of CNTs can have an emissivity greater than 0.98 over a broad wavelength range from the ultraviolet to the THz [140]. These vertically aligned CNT films are the closest demonstration to an ideal black body, making them a useful material as black-body calibration sources. In addition, light emission from CNTs can be strongly polarized if alignment is introduced inside the filament [137]. Furthermore, hot carriers injected under strong bias can lead to the generation of excitons, which then can decay radiatively [141, 142]. Because of the singularities in density of states, this emission due to electron-hole recombination displays resonance features and deviate from Planck's law. Liu and coworkers systematically investigated thermal

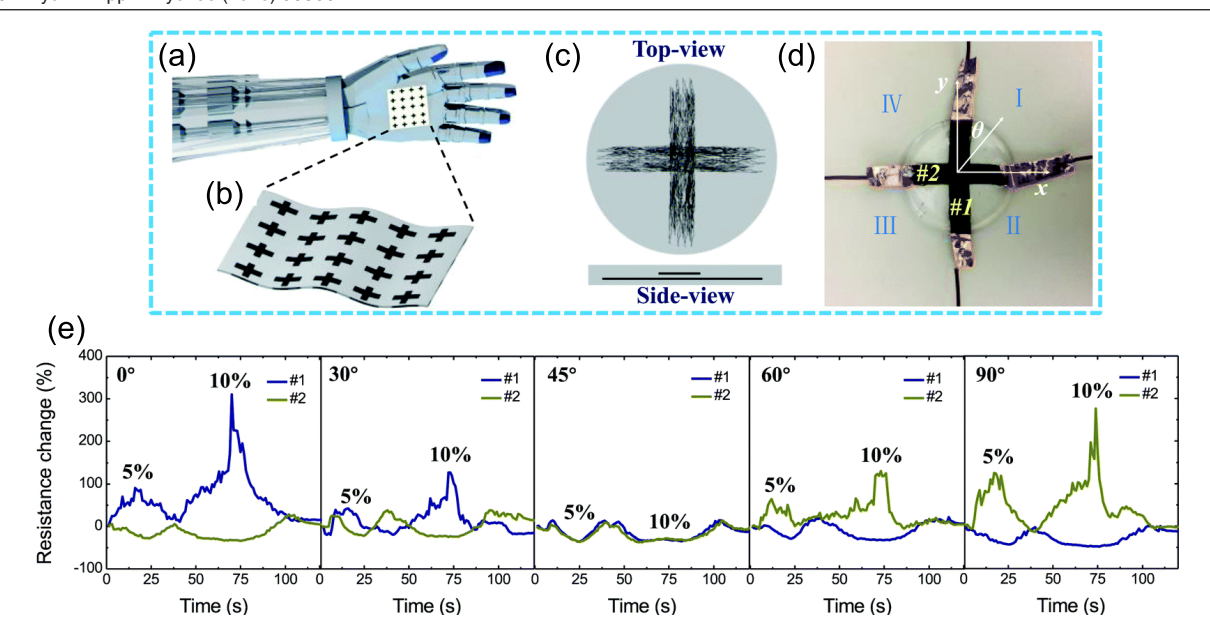


Figure 18. Demonstration of direction sensing. (a) Schematic for a robot arm with an artificial skin. (b) Schematic of the artificial skin with CNT directional sensors. (c) Schematic top and side views of the directional sensor. Two aligned CNT films were assembled to form a cross-like laminated structure. (d) Optical image of a piece of a prepared direction sensor based on aligned CNT films. (e) Response of electrical signal to loading and unloading with strains from different directions. Reproduced from [109] with permission of The Royal Society of Chemistry.

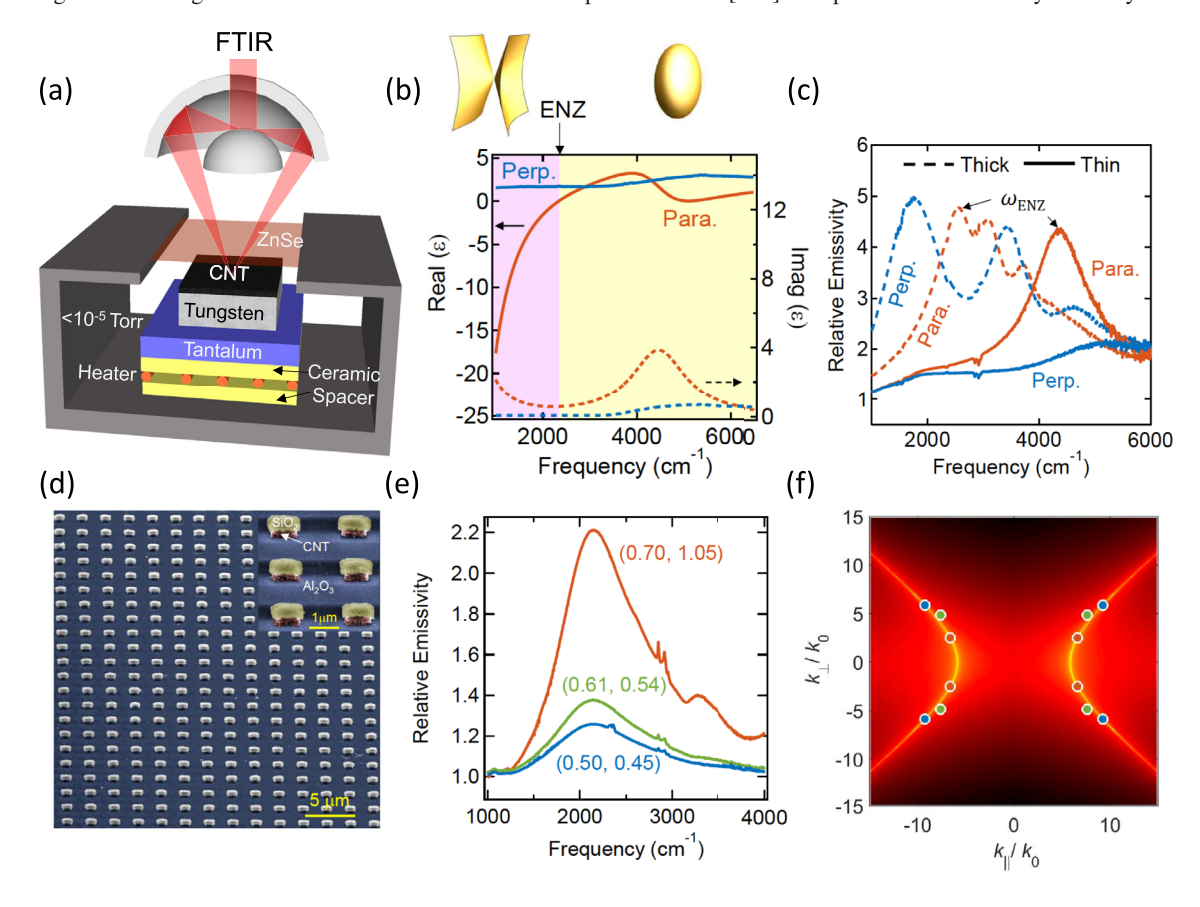


Figure 19. SWCNT hyperbolic thermal emitters. (a) Experimental configuration for thermal emission and reflectivity measurements at temperatures up to 700 °C. (b) The dielectric constants for both parallel and perpendicular directions with respect to the CNT alignment, with an ENZ frequency at $2335\,\mathrm{cm}^{-1}$. (c) Relative emissivity parallel and perpendicular to the CNT alignment directions for a 188 nm thick film and a 1.75 μ m thick film on a tungsten substrate. (d) Representative false-color SEM images of fabricated CNT hyperbolic cavities. The inset shows a closer view of the CNT cavities. (e) Measured relative emissivity from three cavities with different dimensions in μ m. The emission peak at 2140 cm⁻¹ does not shift despite different cavity geometries. (f) The extracted isofrequency contours based on cavities dimensions and dielectric constants. Reprinted with permission from [145]. Copyright © 2019, American Chemical Society.

emission spectra from suspended individual CNTs [143]. For both semiconducting and metallic tubes, in addition to black-body emission tails, strongly polarized spectrally selective thermal emission was observed and the resonance coincided with exciton transition energies in these tubes. It has also been shown that an electrically driven CNT black-body light emitter can be modulated very fast, achieving a speed as high as 1 Gbps [144].

More recently, Gao and coworkers have demonstrated a different mechanism to build spectrally selective thermal emitters based on hyperbolic dispersions in macroscopically aligned CNTs [145]. The extreme anisotropy of optical properties in macroscopically aligned SWCNTs prepared by the CVF technique (see section 2.3) not only led to a hyperbolic dispersion but also enhanced photonic-density of states (PDOS). Direct thermal emission measurements on SWCNT films and architectures were done using a Fourier transform IR spectrometer equipped with a reflective microscope and a controlled resistive heater under vacuum to eliminate any ambiguity of temperature extraction (figure 19(a)). Figure 19(b) plots both the real and imaginary parts of the ordinary and extraordinary dielectric constants in the directions parallel and perpendicular to the CNT alignment direction at 700 °C, which were extracted from reflectance measurements. While the permittivity perpendicular to the CNT alignment direction behaves like a low-loss dielectric over the entire spectral range, the permittivity parallel to the CNT alignment direction exhibits metallic behavior in the mid-IR with an epsilon-near-zero (ENZ) frequency at $2335 \,\mathrm{cm}^{-1}$ (4.3 $\mu\mathrm{m}$). The extreme permittivity anisotropy with respect to the CNT alignment direction below the ENZ frequency creates a hyperbolic dispersion or hyperboloid isofrequency surface, an open surface with an unbounded surface area and hence an unbounded PDOS. On the contrary, the isofrequency surface for frequencies higher than the ENZ frequency is an ellipsoid, a surface with a finite surface area and hence a finite PDOS. Figure 19(c) shows polarization-dependent thermal emission from a 188 nm thick film normalized by the tungsten substrate's relatively flat emissivity spectrum. The prominent peak observed in the parallel polarization case is due to the Berreman modes excited by the impedance matching condition in the multilayer structure. Because this phenomenon does not occur in the perpendicular polarization, there is no enhancement of thermal emission and no corresponding peak.

Because hyperbolic media possess extremely large PDOS, they can support a vastly larger number of thermal photons per unit volume than a black body. Despite the large PDOS, wavevector mismatch prevents some thermal photons from radiating out to far field. Engineering hyperbolic materials at the nanoscale can outcouple some of these photons and provide us with a way to probe high-*k* thermal photons using far-field thermal emission measurements. Thus, sub-wavelength cavities made from hyperbolic materials are expected to resonantly enhance thermal radiation. An array of hyperbolic cavities were fabricated using standard nanofabrication techniques; false-color SEM images are shown in figure 19(d). Pictured in the inset is the 50 nm thick SiO₂ mask, the 500 nm thick patterned layers of aligned CNTs serving as cavities,

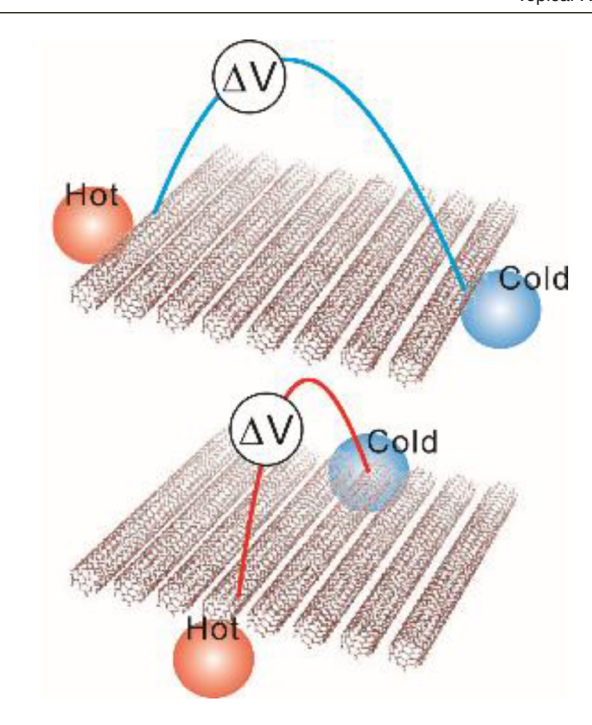


Figure 20. Schematic images of thermoelectric measurement geometries for macroscopically well-aligned CNT films. A voltage induced by a temperature gradient is measured in directions parallel and perpendicular to the CNT alignment direction.

and the 400 nm thick Al_2O_3 film on a tungsten substrate. The resonance frequency of the CNT cavities can remain constant for different cavity dimensions by simultaneously altering dimensions perpendicular and parallel to the direction of CNT alignment, as shown in figure 19(e). Resonant emission occurs at $2140\,\mathrm{cm}^{-1}$ (4.7 $\mu\mathrm{m}$) for all three cavities despite their different geometries. The isofrequency contour of CNTs at this frequency determined based on the cavity dimensions shows excellent agreement with that determined based on the dielectric constants at this frequency (figure 19(f)).

4.2. Thermoelectrics

Waste heat recovery is an important global task since over 25% of industrial and 70% of electrical energy usage is wasted as heat [146]. In addition, there is a growing demand for thermoelectric materials that are flexible and thus ideally suited for flexible electronics and sensors [147]. Low-dimensional materials such as SWCNTs can revolutionize this field by providing a flexible platform with enhanced thermoelectric performance due to singularities in density of states [58, 148, 149]. Excellent thermoelectric properties of SWCNTs have been demonstrated on single-tube levels [150, 151], but how those properties can be preserved in macroscopic SWCNT assemblies has been a long-standing question. Here, we examine the thermoelectric characteristics of macroscopic films of aligned SWCNTs.

The thermoelectric performance of a material is assessed in terms of a dimensionless quantity $ZT = (S^2 \sigma T)/\kappa$. Here, S is the Seebeck coefficient, σ is the electrical conductivity, κ is the thermal conductivity, and T is the average temperature of the system. Theoretical calculations predict that

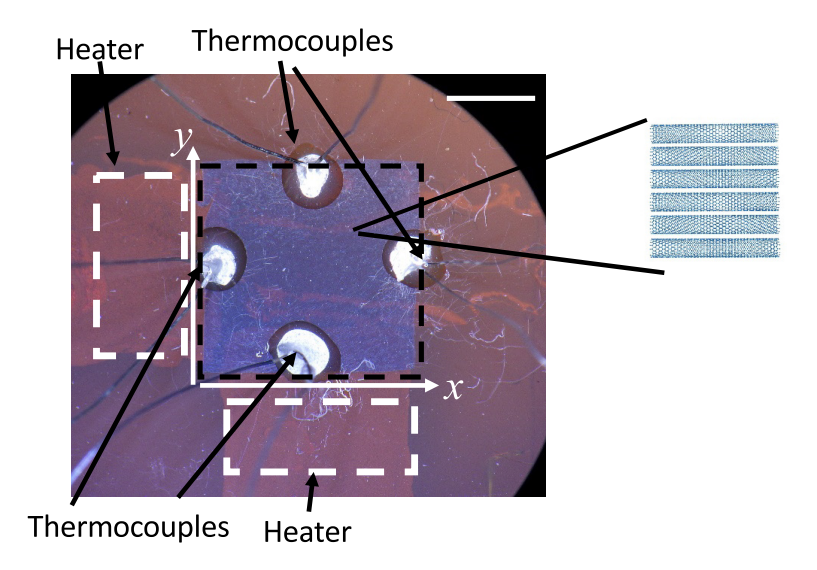


Figure 21. Picture of a device allowing measurements of electrical conductivity and Seebeck coefficient in parallel and perpendicular directions. Heaters outlined by white dashed lines were attached to the back of the substrate. An aligned film of SWCNTs film was transferred onto the area enclosed by the black dashed line, with the tube axis parallel to the *x*-direction. The scale bar is 2 mm. Reprinted from [60], with the permission of AIP Publishing.

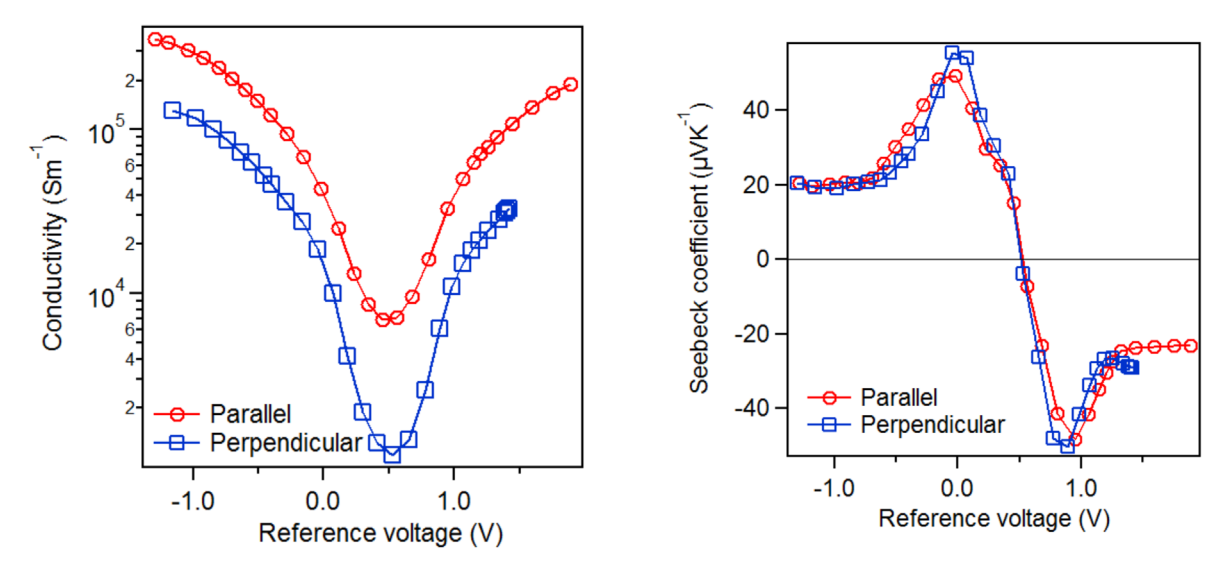


Figure 22. (a) Electrical conductivity and (b) Seebeck coefficient as a function of gate voltage in the parallel (red open circles) and perpendicular (blue open squares) directions in an aligned SWCNT thin film. Reprinted from [60], with the permission of AIP Publishing.

semiconducting SWCNTs should possess very large Seebeck coefficients and large electrical conductivities [152, 153] but moderate ZT factors due to their rather large thermal conductivities. Experimentally reported ZT values have remained very low [59, 154, 155], and thus, there are world-wide efforts to characterize, manipulate, and enhance the thermoelectric properties of macroscopic SWCNT architectures such as films and fibers.

Many factors influence the thermoelectric properties of SWCNT films, such as band structure, chirality, and Fermi level $E_{\rm F}$. In addition, sample morphology strongly influences the thermoelectric performance. Power generation is optimized from a given temperature gradient when the thermoelectric power factor $P = S^2 \sigma$ is maximized. Recent studies have shown that enhancing the power factor requires

high-purity SWCNT films and precise tuning of $E_{\rm F}$ [156–158]. However, the question of how the sample morphology influences thermoelectric performance has remained unanswered. Most of the previous studies on thermoelectric properties of SWCNTs were performed on samples of randomly distributed SWCNTs.

A few studies have investigated thermoelectric properties of SWCNT fibers [159, 160]. For example, Hone *et al* found that before annealing, S was different in the perpendicular and parallel directions, but after annealing S was the same for both directions [159]. Zhou *et al* demonstrated a very high P in a wired assembly of SWCNTs [160]. These studies indicate a strong influence of morphology on the thermoelectric performance of SWCNT assemblies, but it is important to note that both σ and S depend on E_F . Therefore, systematic studies of

the dependence of S on E_F in well-aligned SWCNT films is of vital importance.

Systematically studying thermoelectric properties of aligned SWCNT thin films in well-defined geometries should give us a chance to clarify how the sample morphology influences the thermoelectric performance (figure 20), as recently demonstrated by Fukuhara and coworkers [60]. Figure 21 shows a picture of the experimental setup used. The authors found that the measured Seebeck coefficients in the two directions were both 29 μ V K⁻¹ [60], suggesting an *isotropic* Seebeck coefficient. However, the *S* value strongly depends on E_F , so it is crucial to check the *S* values along parallel and perpendicular directions as a function of E_F . For that purposes, they measured thermoelectric measurements under electrolyte gating [157, 161, 162].

With the electrolyte gating method, one can tune the $E_{\rm F}$ of SWCNTs between plus and minus 1 eV [101], which has been used to reveal new phenomena such as the observation of ISBP absorption [97]; see section 3.1. By combining the electrolyte gating method with thermoelectric measurements, one can investigate how the thermoelectric properties depend on $E_{\rm F}$. Figure 22 shows the σ and S along the parallel and perpendicular directions in an aligned SWCNT thin film (a mixture of metallic and semiconducting SWCNTs). The σ in the parallel direction is clearly larger than that in the perpendicular direction. However, remarkably, the lineshape and values of S in the parallel direction are completely the same as those in the perpendicular direction, clearly indicating the *isotropic* characteristics of S in an anisotropic assembly of aligned SWCNTs.

5. Summary and outlook

In this topical review, we first summarized three ways of fabricating macroscopic ensembles of aligned CNTs—direct growth of aligned CNTs by chemical vapor deposition, production of ultrahigh-conductivity CNT fibers through solution spinning and coating, and spontaneous formation of wafer-scale aligned CNT films via controlled vacuum filtration. These techniques seek to bring the extraordinary properties of individual CNTs to the macroscopic world for diverse applications, especially in flexible and high-temperature electronic and optoelectronic devices. Specifically, we discussed recent studies promising new applications of CNTs using these aligned structures for flexible CNT broadband photodetectors, flexible strain sensors, spectrally selective thermal emitters, and thermoelectric devices.

However, there are still many challenges of best preserving the crystalline, ultralong, and pristine structure of CNTs during macroscopic assembly processes. For example, extensive tip sonication, which is widely used to produce well-dispersed CNT aqueous dispersions, also cuts CNTs and introduces defects, and should be avoided and replaced with other gentle dispersion methods, such as polymer wrapping. New alignment techniques should be also developed for new dispersion methods.

We anticipate that these initial exciting studies will further stimulate much interest in fundamental research on CNTs and accelerate the progress toward real-world applications employing macroscopically aligned CNTs.

Acknowledgments

We thank Xuan Wang, Ahmed Zubair, Chloe F Doiron, and Sakib Hassan for useful discussions. We thank Takuma Makihara for his help with revision process. W G, N K, and J K acknowledge support by the Department of Energy Basic Energy Sciences through Grant No. DE-FG02-06ER46308 (optical spectroscopy experiments), the National Science Foundation through award No. ECCS-1708315 (device fabrication) and the Robert A Welch Foundation through Grant No. C-1509 (sample preparation). L W T was supported by the Department of Defense through the National Defense Science & Engineering Graduate Fellowship (NDSEG) Program. LWT and MP acknowledge support by the Air Force Office of Scientific Research grant FA9550-15-01-0370, the Robert A Welch Foundation grant C-1668, and the Department of Energy (DOE) award DE-EE0007865. K Y acknowledges support by JST CREST through Grant No. JPMJCR17I5, Japan.

ORCID iDs

Weilu Gao https://orcid.org/0000-0003-3139-034X Junichiro Kono https://orcid.org/0000-0002-4195-0577

References

- [1] Kroto H W, Heath J R, O'Brien S C, Curl R F and Smalley R E 1985 *Nature* **318** 162
- [2] Iijima S 1991 Nature **354** 56–8
- [3] Novoselov K S, Geim A K, Morozov S, Jiang D, Zhang Y, Dubonos S, Grigorieva I and Firsov A 2004 Science 306 666-9
- [4] Saito R, Dresselhaus G and Dresselhaus M S 1998 Physical Properties of Carbon Nanotubes (London: Imperial College Press)
- [5] Dresselhaus M S, Dresselhaus G and Avouris P (ed) 2001 Carbon Nanotubes: Synthesis, Structure, Properties, and Applications (Topics in Applied Physics) (Berlin: Springer)
- [6] Reich S, Thomsen C and Maultzsch J 2004 Carbon Nanotubes: Basic Concepts and Physical Properties (Weinheim: Wiley)
- [7] O'Connell M J (ed) 2006 Carbon Nanotubes: Properties and Applications (Boca Raton, FL: CRC Press)
- [8] Jorio A, Dresselhaus G and Dresselhaus M S (ed) 2008 Carbon Nanotubes: Advanced Topics in the Synthesis, Structure, Properties and Applications (Berlin: Springer)
- [9] Nanot S, Thompson N A, Kim J H, Wang X, Rice W D, Hároz E H, Ganesan Y, Pint C L and Kono J 2013 Handbook of Nanomaterials ed R Vajtai (Berlin: Springer) pp 105–46
- [10] Weisman R B and Kono J (ed) 2019 Optical Properties of Carbon Nanotubes: A Volume Dedicated to the Memory of Professor Mildred Dresselhaus (Singapore: World Scientific)
- [11] Iijima S and Ichihashi T 1993 *Nature* **363** 603–5

- [12] Bethune D S, Klang C H, de Vries M S, Gorman G, Savoy R, Vazquez J and Beyers R 1993 Nature 363 605–7
- [13] Kane C L and Mele E J 1997 Phys. Rev. Lett. 78 1932-5
- [14] Kane C, Balents L and Fisher M P A 1997 Phys. Rev. Lett. 79 5086–9
- [15] Balents L and Egger R 2000 Phys. Rev. Lett. 85 3464-7
- [16] Balents L 2000 Phys. Rev. B 61 4429–32
- [17] De Martino A, Egger R, Hallberg K and Balseiro C A 2002 Phys. Rev. Lett. 88 206402
- [18] Levitov L S and Tsvelik A M 2003 Phys. Rev. Lett. 90 016401
- [19] Bellucci S, González J and Onorato P 2005 Phys. Rev. Lett. 95 186403
- [20] Guinea F 2005 Phys. Rev. Lett. 94 116804
- [21] Dóra B, Gulácsi M, Simon F and Kuzmany H 2007 Phys. Rev. Lett. 99 166402
- [22] Dóra B, Gulácsi M, Koltai J, Zólyomi V, Kürti J and Simon F 2008 Phys. Rev. Lett. 101 106408
- [23] Mkhitaryan V V, Fang Y, Gerton J M, Mishchenko E G and Raikh M E 2008 *Phys. Rev. Lett.* **101** 256401
- [24] Mishchenko E G and Starykh O A 2011 Phys. Rev. Lett. 107 116804
- [25] Avouris P, Chen Z and Perebeinos V 2007 Nat. Nanotechnol. 2 605–15
- [26] Avouris P, Freitag M and Perebeinos V 2008 Nat. Photon. 2 341–50
- [27] Nanot S, Hároz E H, Kim J H, Hauge R H and Kono J 2012 Adv. Mater. 24 4977–94
- [28] Liew K, Wong C, He X and Tan M 2005 *Phys. Rev.* B **71** 075424
- [29] Zhang M, Yudasaka M, Koshio A and Iijima S 2002 Chem. Phys. Lett. 364 420-6
- [30] Bom D, Andrews R, Jacques D, Anthony J, Chen B, Meier M S and Selegue J P 2002 Nano Lett. 2 615–9
- [31] Hamada N, Sawada S and Oshiyama A 1992 Phys. Rev. Lett. 68 1579–81
- [32] Hároz E H, Duque J G, Tu X, Zheng M, Walker A R H, Hauge R H, Doorn S K and Kono J 2013 Nanoscale 5 1411–39
- [33] Tans S J, Devoret M H, Dai H, Thess A, Smalley R E, Geerligs L J and Dekker C 1997 *Nature* **386** 474–7
- [34] Ando T and Nakanishi T 1998 *J. Phys. Soc. Japan* **67** 1704–13
- [35] Ando T, Nakanishi T and Saito R 1998 *J. Phys. Soc. Japan* **67** 2857–62
- [36] Dürkop T, Getty S, Cobas E and Fuhrer M 2004 *Nano Lett.* 4 35–9
- [37] Wu Z et al 2004 Science 305 1273-6
- [38] Wang F, Itkis M E, Bekyarova E and Haddon R C 2013 *Nat. Photon.* **7** 459
- [39] Iijima S, Brabec C, Maiti A and Bernholc J 1996 J. Chem. Phys. 104 2089–92
- [40] Falvo M R, Clary G, Taylor Ii R, Chi V, Brooks F Jr, Washburn S and Superfine R 1997 Nature 389 582
- [41] Yakobson B I, Brabec C and Bernholc J 1996 Phys. Rev. Lett. 76 2511
- [42] Yu M F, Files B S, Arepalli S and Ruoff R S 2000 *Phys. Rev. Lett.* **84** 5552
- [43] Yu M F, Lourie O, Dyer M J, Moloni K, Kelly T F and Ruoff R S 2000 *Science* **287** 637–40
- [44] Peng B, Locascio M, Zapol P, Li S, Mielke S L, Schatz G C and Espinosa H D 2008 Nat. Nanotechnol. 3 626
- [45] Xu F, Wu M Y, Safron N S, Roy S S, Jacobberger R M, Bindl D J, Seo J H, Chang T H, Ma Z and Arnold M S 2014 Nano Lett. 14 682–6
- [46] Chen Y, Zhan H, Shi Q Q, Wu G and Wang J N 2019 *Nanotube* Superfiber Materials (Amsterdam: Elsevier) pp 65–76
- [47] Alzaid M, Taufique A M, Thomas S A, Carufel C, Harris J M, Waters A J, Altayyar A, May S and Hobbie E K 2018 Langmuir 34 7951–7

- [48] Bai Y et al 2018 Nat. Nanotechnol. 13 589
- [49] Dai H, Hafner J H, Rinzler A G, Colbert D T and Smalley R E 1996 Nature 384 147
- [50] Wang C, Takei K, Takahashi T and Javey A 2013 Chem. Soc. Rev. 42 2592–609
- [51] Cao Q, Kim H S, Pimparkar N, Kulkarni J P, Wang C, Shim M, Roy K, Alam M A and Rogers J A 2008 Nature 454 495
- [52] LeMieux M C, Roberts M, Barman S, Jin Y W, Kim J M and Bao Z 2008 Science 321 101–4
- [53] Sun D M, Timmermans M Y, Tian Y, Nasibulin A G, Kauppinen E I, Kishimoto S, Mizutani T and Ohno Y 2011 Nat. Nanotechnol. 6 156
- [54] Wang C, Zhang J and Zhou C 2010 ACS Nano 4 7123-32
- [55] Wang C, Chien J C, Takei K, Takahashi T, Nah J, Niknejad A M and Javey A 2012 Nano Lett. 12 1527–33
- [56] Yu Z, Niu X, Liu Z and Pei Q 2011 Adv. Mater. 23 3989-94
- [57] Lipomi D J, Vosgueritchian M, Tee B C, Hellstrom S L, Lee J A, Fox C H and Bao Z 2011 Nat. Nanotechnol. 6 788
- [58] Hicks L D and Dresselhaus M S 1993 Phys. Rev. B 47 16631-4
- [59] Avery A D et al 2016 Nat. Energy 1 16033
- [60] Fukuhara K, Ichinose Y, Nishidome H, Yomogida Y, Katsutani F, Komatsu N, Gao W, Kono J and Yanagi K 2018 Appl. Phys. Lett. 113 243105
- [61] Blackburn J L, Ferguson A J, Cho C and Grunlan J C 2018 Adv. Mater. 30 1704386
- [62] Du Y, Xu J, Paul B and Eklund P 2018 Appl. Mater. Today 12 366–88
- [63] Zevalkink A et al 2018 Appl. Phys. Rev. 5 021303
- [64] Murakami Y, Miyauchi Y, Chiashi S and Maruyama S 2003 Chem. Phys. Lett. 377 49–54
- [65] Murakami Y, Chiashi S, Miyauchi Y, Hu M, Ogura M, Okubo T and Maruyama S 2004 Chem. Phys. Lett. 385 298–303
- [66] Hata K, Futaba D N, Mizuno K, Namai T, Yumura M and Iijima S 2004 Science 306 1362–5
- [67] Pint C L, Pheasant S T, Parra-Vasquez A N G, Horton C, Xu Y and Hauge R H 2009 J. Phys. Chem. C 113 4125–33
- [68] Pint C L, Xu Y, Pasquali M and Hauge R H 2008 ACS Nano 2 1871–8
- [69] Pint C L et al 2010 ACS Nano 4 1131-45
- [70] Ramesh S, Ericson L M, Davis V A, Saini R K, Kittrell C, Pasquali M, Billups W, Adams W W, Hauge R H and Smalley R E 2004 J. Phys. Chem. B 108 8794–8
- [71] Davis V Å et al 2009 Nat. Nanotechnol. 4 830-4
- [72] Pagani G, Green M J, Poulin P and Pasquali M 2012 Proc. Natl Acad. Sci. USA 109 11599–604
- [73] Saini R K, Chiang I W, Peng H, Smalley R, Billups W, Hauge R H and Margrave J L 2003 J. Am. Chem. Soc. 125 3617–21
- [74] Ericson L M et al 2004 Science 305 1447–50
- [75] Behabtu N et al 2013 Science 339 182-6
- [76] Tsentalovich D E, Headrick R J, Mirri F, Hao J, Behabtu N, Young C C and Pasquali M 2017 ACS Appl. Mater. Interfaces 9 36189–98
- [77] Rodger A and Nordén B 1997 Circular Dichroism and Linear Dichroism (Oxford: Oxford University Press)
- [78] Katsutani F, Gao W, Li X, Ichinose Y, Yomogida Y, Yanagi K and Kono J 2019 Phys. Rev. B 99 035426
- [79] Headrick R J, Tsentalovich D E, Berdegué J, Bengio E A, Liberman L, Kleinerman O, Lucas M S, Talmon Y and Pasquali M 2018 Adv. Mater. 30 1704482
- [80] He X et al 2016 Nat. Nanotechnol. 11 633-8
- [81] Gao W and Kono J 2019 R. Soc. Open Sci. 6 181605
- [82] Komatsu N, Gao W, Chen P, Guo C, Babakhani A and Kono J 2017 Adv. Funct. Mater. 27 1606022
- [83] Graupner R, Abraham J, Vencelova A, Seyller T, Hennrich F, Kappes M M, Hirsch A and Ley L 2003 Phys. Chem. Chem. Phys. 5 5472–6

- [84] Tantang H, Ong J Y, Loh C L, Dong X C, Chen P, Chen Y, Hu X, Tan L P and Li L J 2009 *Carbon* 47 1867–70
- [85] Skakalova V, Kaiser A B, Dettlaff-Weglikowska U, Hrncarikova K and Roth S 2005 J. Phys. Chem. B 109 7174–81
- [86] He X et al 2014 Nano Lett. 14 3953-8
- [87] Yang L, Wang S, Zeng Q, Zhang Z and Peng L M 2013 Small 9 1225–36
- [88] He X, Léonard F and Kono J 2015 Adv. Opt. Mater. 3 989–1011
- [89] Richter M, Heumüller T, Matt G J, Heiss W and Brabec C J 2017 Adv. Energy Mater. 7 1601574
- [90] Zeng Q et al 2012 Opt. Mater. Express 2 839-48
- [91] Balestrieri M et al 2017 Adv. Funct. Mater. 27 1702341
- [92] Wang S, Zhang Z, Ding L, Liang X, Shen J, Xu H, Chen Q, Cui R, Li Y and Peng L M 2008 Adv. Mater. 20 3258–62
- [93] Wang S et al 2009 J. Phys. Chem. C 113 6891-3
- [94] Zeng Q, Wang S, Yang L, Wang Z, Zhang Z, Peng L, Zhou W and Xie S 2012 Nano Res. 5 33–42
- [95] Barkelid M and Zwiller V 2014 Nat. Photon. 8 47–51
- [96] Levine B F 1993 J. App. Phys. 74 R1-81
- [97] Yanagi K, Okada R, Ichinose Y, Yomogida Y, Katsutani F, Gao W and Kono J 2018 Nat. Commun. 9 1121
- [98] Kazaoui S, Minami N, Jacquemin R, Kataura H and Achiba Y 1999 *Phys. Rev.* B **60** 13339–42
- [99] Kim K K et al 2008 J. Am. Chem. Soc. 130 12757-61
- [100] Yanagi K, Moriya R, Yomogida Y, Takenobu T, Naitoh Y, Ishida T, Kataura H, Matsuda K and Maniwa Y 2011 Adv. Mater. 23 2811–4
- [101] Igarashi T, Kawai H, Yanagi K, Cuong N T, Okada S and Pichler T 2015 Phys. Rev. Lett. 114 176807
- [102] Nanot S, Cummings A W, Pint C L, Ikeuchi A, Akiho T, Sueoka K, Hauge R H, Léonard F and Kono J 2013 Sci. Rep. 3 1335
- [103] He X, Nanot S, Wang X, Hauge R H, Kane A A,
 Goldsmith J E M, Léonard F and Kono J 2013 ACS Nano
 7 7271-7
- [104] Zubair A, Wang X, Mirri F, Tsentalovich D E, Fujimura N, Suzuki D, Soundarapandian K P, Kawano Y, Pasquali M and Kono J 2018 Phys. Rev. Mater. 2 015201
- [105] Yamada T, Hayamizu Y, Yamamoto Y, Yomogida Y, Izadi-Najafabadi A, Futaba D N and Hata K 2011 Nat. Nanotechnol. 6 296
- [106] Yu Y, Luo Y, Guo A, Yan L, Wu Y, Jiang K, Li Q, Fan S and Wang J 2017 *Nanoscale* 9 6716–23
- [107] Zhao H, Zhang Y, Bradford P D, Zhou Q, Jia Q, Yuan F G and Zhu Y 2010 Nanotechnology 21 305502
- [108] Ryu S, Lee P, Chou J B, Xu R, Zhao R, Hart A J and Kim S G 2015 ACS Nano 9 5929–36
- [109] Sui C et al 2018 Nanoscale 10 14938-46
- [110] Khang D Y, Jiang H, Huang Y and Rogers J A 2006 Science 311 208–12
- [111] Kim D H, Ahn J H, Choi W M, Kim H S, Kim T H, Song J, Huang Y Y, Liu Z, Lu C and Rogers J A 2008 Science 320 507–11
- [112] Sekitani T, Noguchi Y, Hata K, Fukushima T, Aida T and Someya T 2008 *Science* **321** 1468–72
- [113] Chen Z, Ren W, Gao L, Liu B, Pei S and Cheng H M 2011 Nat. Mater. 10 424
- [114] Kim D H et al 2011 Science 333 838-43
- [115] Jung Y J et al 2006 Nano Lett. 6 413-8
- [116] Yan C, Kang W, Wang J, Cui M, Wang X, Foo C Y, Chee K J and Lee P S 2013 ACS Nano 8 316–22
- [117] Melzer M et al 2015 Adv. Mater. 27 1274-80
- [118] Tombler T W, Zhou C, Alexseyev L, Kong J, Dai H, Liu L, Jayanthi C, Tang M and Wu S Y 2000 Nature 405 769

- [119] Cao J, Wang Q and Dai H 2003 Phys. Rev. Lett. 90 157601
- [120] Minot E, Yaish Y, Sazonova V, Park J Y, Brink M and McEuen P L 2003 Phys. Rev. Lett. 90 156401
- [121] Grow R J, Wang Q, Cao J, Wang D and Dai H 2005 Appl. Phys. Lett. 86 093104
- [122] Stampfer C, Jungen A, Linderman R, Obergfell D, Roth S and Hierold C 2006 Nano Lett. 1449–53
- [123] Nishio T, Miyato Y, Kobayashi K, Matsushige K and Yamada H 2008 Appl. Phys. Lett. 92 063117
- [124] Li Z, Dharap P, Nagarajaiah S, Barrera E V and Kim J 2004 *Adv. Mater.* **16** 640–3
- [125] Dharap P, Li Z, Nagarajaiah S and Barrera E 2004 Nanotechnology 15 379
- [126] Li X, Levy C and Elaadil L 2008 Nanotechnology 19 045501
- [127] Shin M K, Oh J, Lima M, Kozlov M E, Kim S J and Baughman R H 2010 Adv. Mater. 22 2663–7
- [128] Lee J I, Pyo S, Kim M O and Kim J 2018 Nanotechnology 29 055501
- [129] Jiang K, Li Q and Fan S 2002 Nature 419 801
- [130] Jiang K, Wang J, Li Q, Liu L, Liu C and Fan S 2011 *Adv. Mater.* **23** 1154–61
- [131] Zhang Y, Zou G, Doorn S K, Htoon H, Stan L, Hawley M E, Sheehan C J, Zhu Y and Jia Q 2009 ACS Nano 3 2157–62
- [132] Lochbaum A, Fedoryshyn Y, Dorodnyy A, Koch U, Hafner C and Leuthold J 2017 ACS Photon. 4 1371–80
- [133] Lenert A, Bierman D M, Nam Y, Chan W R, Celanović I, Soljačić M and Wang E N 2014 *Nat. Nanotechnol.* 9 126
- [134] Yudasaka M, Kataura H, Ichihashi T, Qin L C, Kar S and Iijima S 2001 *Nano Lett.* **1** 487–9
- [135] Akima N et al 2006 Adv. Mater. 18 1166-9
- [136] Sveningsson M, Jönsson M, Nerushev O, Rohmund F and Campbell E 2002 *Appl. Phys. Lett.* **81** 1095–7
- [137] Li P, Jiang K, Liu M, Li Q, Fan S and Sun J 2003 Appl. Phys. Lett. 82 1763–5
- [138] Wei J, Zhu H, Wu D and Wei B 2004 *Appl. Phys. Lett.* **84** 4869–71
- [139] Itkis M E, Yu A and Haddon R C 2008 Nano Lett. 8 2224-8
- [140] Mizuno K, Ishii J, Kishida H, Hayamizu Y, Yasuda S, Futaba D N, Yumura M and Hata K 2009 Proc. Natl Acad. Sci. USA 106 6044–7
- [141] Chen J, Perebeinos V, Freitag M, Tsang J, Fu Q, Liu J and Avouris P 2005 Science 310 1171–4
- [142] Mann D, Kato Y, Kinkhabwala A, Pop E, Cao J, Wang X, Zhang L, Wang Q, Guo J and Dai H 2007 Nat. Nanotechnol. 2 33–8
- [143] Liu Z, Bushmaker A, Aykol M and Cronin S B 2011 ACS Nano 5 4634–40
- [144] Mori T, Yamauchi Y, Honda S and Maki H 2014 Nano Lett. 14 3277–83
- [145] Gao W, Doiron C, Li X, Kono J and Naik G V 2019 ACS Photon. 6 1602–9
- [146] Gingerich D B and Mauter M S 2015 *Environ. Sci. Technol.* **49** 8297–306
- [147] Bahk J H, Fang H, Yazawa K and Shakouri A 2015 J. Mater. Chem. C 3 10362–74
- [148] Hicks L, Harman T, Sun X and Dresselhaus M 1996 Phys. Rev. B 53 R10493
- [149] Mahan G D and Sofo J O 1996 *Proc. Natl Acad. Sci.* **93** 7436–9
- [150] Small J P, Perez K M and Kim P 2003 *Phys. Rev. Lett.* **91** 256801
- [151] Llaguno M C, Fischer J E, Johnson A T and Hone J 2004 Nano Lett. 4 45–9
- [152] Jiang J W, Wang J S and Li B 2011 J. Appl. Phys. 109 014326
- [153] Hung N T, Nugraha A R T, Hasdeo E H, Dresselhaus M S and Saito R 2015 Phys. Rev. B 92 165426

- [154] Norton-Baker B, Ihly R, Gould I E, Avery A D, Owczarczyk Z R, Ferguson A J and Blackburn J L 2016 ACS Energy Lett. 1 1212–20
- [155] MacLeod B A et al 2017 Energy Environ. Sci. 10 2168-79
- [156] Nakai Y, Honda K, Yanagi K, Kataura H, Kato T, Yamamoto T
- and Maniwa Y 2014 *Appl. Phys. Express* **7** 025103 [157] Yanagi K, Kanda S, Oshima Y, Kitamura Y, Kawai H, Yamamoto T, Takenobu T, Nakai Y and Maniwa Y 2014 Nano Lett. 14 6437-42
- [158] Ichinose Y et al 2019 Nano Lett. 19 7370-6
- [159] Hone J, Llaguno M, Nemes N, Johnson A, Fischer J, Walters D, Casavant M, Schmidt J and Smalley R 2000 Appl. Phys. Lett. 77 666-8
- [160] Zhou W et al 2016 Small 12 3407–14
- [161] Oshima Y, Kitamura Y, Maniwa Y and Yanagi K 2015 Appl. Phys. Lett. 107 043106
- [162] Shimizu S, Iizuka T, Kanahashi K, Pu J, Yanagi K, Takenobu T and Iwasa Y 2016 Small 12 3388-92